Numerical Simulation of Contemporary Kinematics at the Northeastern Tibetan Plateau and its implications for seismic hazard assessment

Liming Li[1,2], Xianrui Li[3], Fanyan Yang[2], Lili Pan[4], Jingxiong Tian[2]

[1] School of Earth Sciences and Resources, China University of Geosciences (Beijing), Beijing 100083, China.

[2] Ningxia Institute of Geological Survey, Yinchuan, Ningxia 750021, China.

[3] Department of Earth and Space Sciences, Southern University of Science and Technology, Shenzhen 518055, China.

[4] School of Earth Sciences and Engineering, Sun Yat-Sen University, Zhuhai 519082, China.

Corresponding to: Liming Li (cugliming@cug.edu.cn)

Abstract. The slip rates of active faults at the northeastern Tibetan Plateau (NETP) should be clarified to understand the lateral expansion of the Tibetan Plateau and assess the seismic hazards in this region. To obtain the continuous slip rates of active faults at the NETP, we constructed a three-dimensional geomechanics-numerical model which includes a complex 3D fault system. The model also accounts for the physical rock properties, gravity fields, fault friction coefficients, initial stress and boundary conditions. Then we presented the long-term kinematics of NETP according to the horizontal and vertical velocities and fault slip rates acquired from the model. The fault kinematic characteristics indicate that the Laohushan, middle–southern Liupanshan, and Guguan–Baoji faults, as well as the junction area of the Maxianshan and Zhuanglanghe faults are potential hazard areas for strong earthquakes. However, as these faults are currently in the stress accumulation stage, they are unlikely to cause a strong earthquake in the short term. In contrast, it is likely that the Jinqiangshan–Maomaoshan fault will generate a M_S 7.1–7.3 earthquake in the coming decades. In addition, the velocity profiles across the NETP imply that the plate rotation is the primary mechanism for the deformation of the NETP even though the intrablock straining and faulting are non-negligible.

1 Introduction

The northeastern Tibetan Plateau (NETP) is the growth front of the Tibetan Plateau (TP). Modern geomorphology and tectonic features of the NETP are inferred to be formed due to the expansion of the TP toward its periphery, which has been ongoing since the Indian and Eurasian plates collided (P. Zhang et al., 2013, 2014). Having experienced the strong Cenozoic deformation, crust of this area develops a complex fault system with several large and deep faults, such as the generalized Haiyuan fault (F1), West Ordos fault (F2), West Qinling fault (F3), East Kunlun fault (F4), that divide the NETP into the Alxa, Ordos, Qilian, Qaidam, and Bayan Har blocks (Zhang et al., 2003; Fig.1). These faults are characterized by extremely intense tectonic movements and seismic activities (Zhang, 1999; Zheng et al., 2016b). At least 5 earthquakes with magnitudes of ≥ 8, such as the 1654 M 8.0 Tianshui, 1739 M 8.0 Pingluo, 1879 M 8.0 Wudu, 1920 M 8.0 Haiyuan, and 1927 M 8.0 Gulang earthquakes, occurred in this area and caused huge loss of life and property in history (Fig. 1). Since the generation and magnitude of an earthquake is closely related to fault

activity, long-term fault slip rate plays a key role in medium- and long-term seismic hazard assessment (Ding et al.,
1993; Xu et al., 2018). For example, combined with coseismic displacements, long-term fault slip rates can be used
to calculate earthquake recurrence interval (Shen et al., 2009) and assess the magnitudes of potential earthquakes (Bai
et al., 2018; Hergert and Heidbach, 2010). Moreover, the spatially continuous fault slip rates, which are lack in the
NETP, can also be used to reconstruct the tectonic evolution of this area and provide important insights into the lateral
expansion pattern and deformation mechanisms of the TP (Royden et al., 1997; Tapponnier et al., 1982; Zhang et al.,
2004).

Although there has been extensive research on the fault slip rates in the NETP by using geologic (Chen et al., 2019;
Li et al., 2009; Li et al., 2018; Matrau et al., 2019; Wang et al., 2021;X. Li et al., 2017) or geodetic (Hao et al., 2021;
Li, Pierce, et al., 2021; X. Li et al., 2019) approaches, a systematic mismatch is typically found between the slip rates
calculated from geological records and that obtained from geodetic inversion, due to the limited assumptions behind
these two methods. For example, the geological slip rates only represent the activities of one fault branch that measured
in a fault zone, which is always consist of several branches. They are usually lower than the geodetic slip rates on the
fault as a whole if a rigid block assumption is adopted in the geodetic inversion process (Shen et al., 2009). However,
several crustal deformation studies conducted in TP demonstrated that the internal block deformation in the NETP
cannot be ignored (Royden et al., 1997; Zhang et al., 2004; Y. Li et al., 2017, 2021). Numerical modeling provides a
powerful tool to study the large-scale crustal kinematics (Hergert and Heidbach, 2010; Hergert et al., 2011) as well as
the comprehensive 3D view of fault activities with spatially continuous distribution. High efficiency and accuracy
have made the numerical modeling a widespread technology in the field of geosciences, especially for the study of
kinematics and dynamics of the NETP (Pang et al., 2019a, b; Sun et al., 2018, 2019; Zhu et al., 2018; Xiao and He,
2015). However, all these previous numerical models are either two-dimensional (2D) or three-dimensional (3D) with
extremely simplified fault planes. To our knowledge, so far there is no 3D geomechanical model that take into the
complex 3D fault system in the NETP. Therefore, detailed kinematics of the crust and faults in the NETP still remains
unclear.

In this study, instead of a simple conceptual model, a comprehensive 3D geomechanical model of the NETP with
detailed complex 3D fault geometries, heterogeneous rock properties and reasonable initial crustal stress is constructed.
After calibrated by model-independent observations, the results of the geomechannical model, such as the horizontal
crustal velocities, spatially continuous slip rates of major faults, are presented. Based on these results, we summarized
the long-term crustal deformation characteristics in the NETP. Finally, we assessed the seismic hazards of major faults
in the study area, and suggested that the Jinqiangshan–Maomaoshan fault has the potential for a M_S 7.1–7.3 earthquake
in the coming decades.
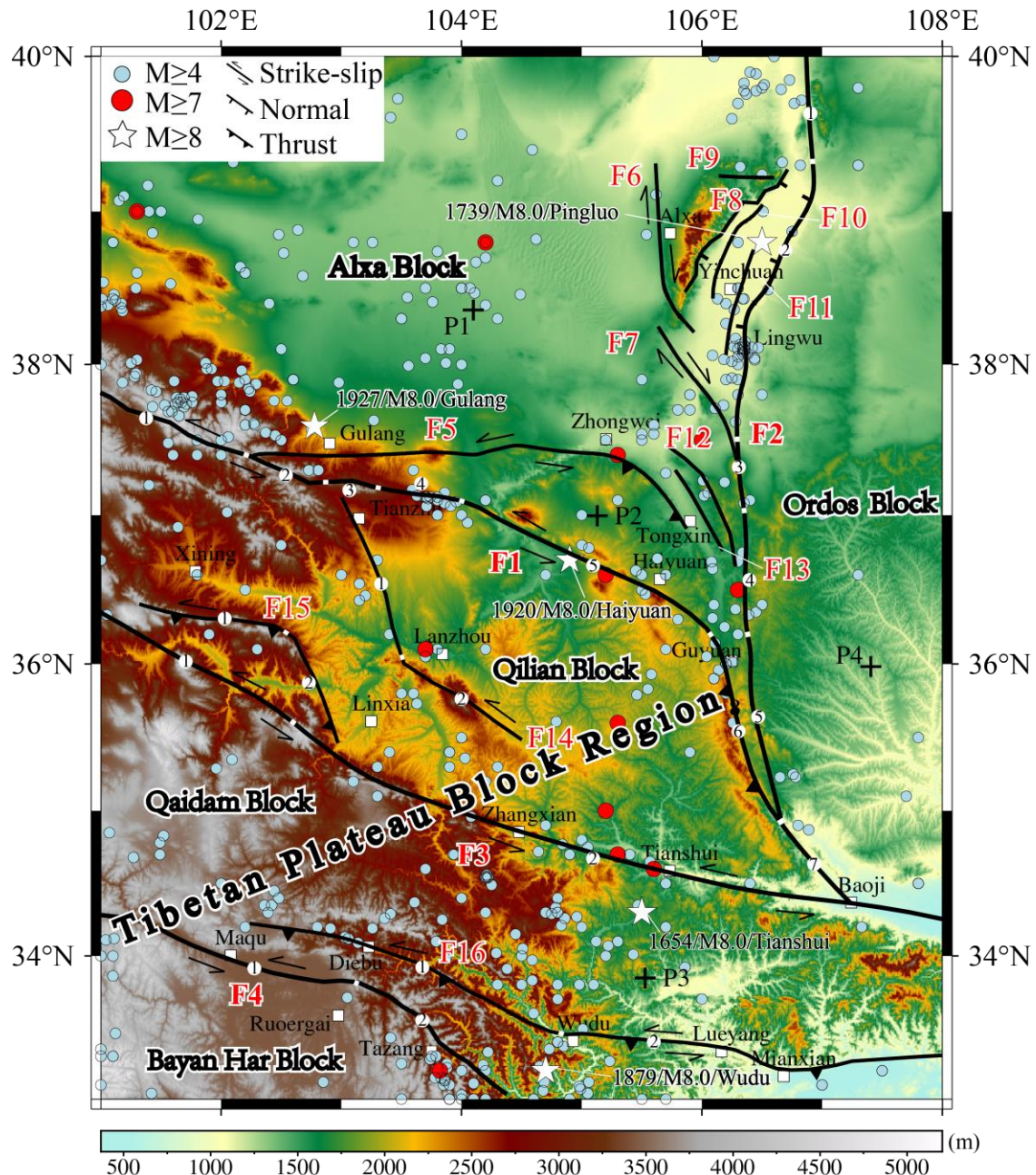
Figure 1. Map of active faults and earthquakes of the NETP. Black lines represent the active faults. The light blue, red dots and the white pentagrams represent earthquakes from 1831 BC to 2017 AD from the National Earthquake Data Center (http://data.earthquake.cn). Black crosses (P1-P4) indicate the locations of four test sites for the comparison with the numerical model shown in Fig. 3b. Faults discussed in the text are labeled as followed: F1-1 = LLLF = Lenglongling fault; F1-2 = JQHF = Jinqinaghe fault; F1-3 = MMSF = Maomaoshan fault; F1-4 = LHSF = Laohushan fault; F1-5 = HYF = Haiyuan fault. F1-6 = LPSF = Liupanshan fault; F1-7=GG-BJF=Guguan-Baoji fault; F2-1 = ZZSF = Zhuozishan fault; F2-2 = HHF = Huanghe fault; F2-3 = LSF = Luoshan fault; F2-4 = YWSF = Yunwushan fault; F2-5 = XGSF = Xiaoguanshan fault; F3-1 = DTH-LXF = Daotanghe–Linxia fault; F3-2 = WQLF = West Qinling fault. F4-1 = EKLF = Eastern Kunlun fault; F4-2 = TZF = Tazang fault; F5 = TJSF = Tianjingshan fault; F6 = WHLSF = West Helanshan fault; F7 = NSSF = Niushoushan fault; F8 = EHLSF = East Helanshan fault; F9 = ZYGF = Zhengyiguan fault; F10 = LHTF = Lvhuatai fault; F11 = YCF = Yinchuan fault; F12 = YTSF = Yantongshan fault; F13 = QSHF = Qingshuihe fault; F14-1 = ZLSF = Zhuanglanghe fault; F14-2 = MXSF=Maxianshan fault. F15-1 = WLJSF = West Lajishan fault; F15-2 = ELJSF = East Lajishan fault; F16-1 = DB-BLJF = Diebu–Bailongjiang fault; F16-2 = WD-KXF = Wudu–Kangxian fault.

2 Model concept and input

2.1 Model geometry

The 3D geomechanics model of this work is a rectangular cartesian 3D block with an E–W length of 654 km (101°E–108°E), N–S length of 777 km (33°N–40°N), and thickness of ~80 km. The topography of the model's surface is based on GTOPO30 elevation data, which has a resolution of 30 arcseconds (about 900m). The model comprises four layers: the upper crust, middle crust, lower crust, and upper mantle, from top to bottom. The geometric data of the layer interfaces were derived from CRUST1.0 (Laske et al., 2013).

Based on their depth, the faults of the model can be categorized into lithospheric and crustal faults. Lithospheric faults (i.e., F1, F2, F3, and F4) cut through the Moho and reach the bottom of the model (Zhan et al., 2005; B. Liu et al., 2017; Zhao et al., 2015; Fig. 2a, b; Table 1). All other faults are crustal faults that terminate in the upper, middle, or lower crust (Yuan et al., 2002b, 2003; Lease et al., 2012; Meng et al., 2012; B. Liu et al., 2017; Wu et al., 2020). The fault traces are modified from Xu et al. (2016) and the attitudes of these faults are summarized from previously published data including surface fault surveys and deep seismic profiles (Table 1). In the NETP, many geophysical investigations found that low-velocity bodies exist widely in the middle-lower crust and deformations in the upper crust are not coupled to those in the middle-lower crust (Bao et al., 2013; Wang et al., 2018; Ye et al., 2016). Therefore, we introduced a contact surface between the upper and middle crusts into the model and account it as a detachment layer that make the upper crust decouple from the middle crust and allow the upper crust sliding freely along the contact surface according to the stress conditions.

The model was meshed using tetrahedron elements. The element size is 1–2 km near the faults and increases to ~10 km at the model boundary. The model totally contained 8,463,583 elements (Fig. 2a).

2.2 Rock properties

In order to obtain the time-independent contemporary background crustal stress of the NETP, we assumed that the rock rheology in the model is linear elasticity, consistent with the observations that the large-scale continental crust always exhibits elastic-brittle behavior rather than elastic-viscous behavior (Armijo et al., 2004; Hubert-Ferrari et al., 2003). The model was divided into three major tectonic units—the Alxa block, the Ordos block, and the TP block region. The part of the TP block region that located in the study area comprises the Qilian, Qaidam, and Bayan Har blocks. The rock properties of each block contain the elastic parameters (i.e. the Young's modulus, density, and Poisson's ratio) of the upper, middle, and lower crust as well as those of the upper mantle (Fig. 2a). The density and Poisson's ratio were derived from CRUST1.0 (Laske et al., 2013). The Young's modulus adopted in our model is static and was converted from the dynamic elastic modulus using the empirical equation of Brotons et al. (2016), which was calculated based on the P-wave velocities, S-wave velocities, and densities derived from CRUST1.0. The elastic parameters used in the model are listed in Table 2.
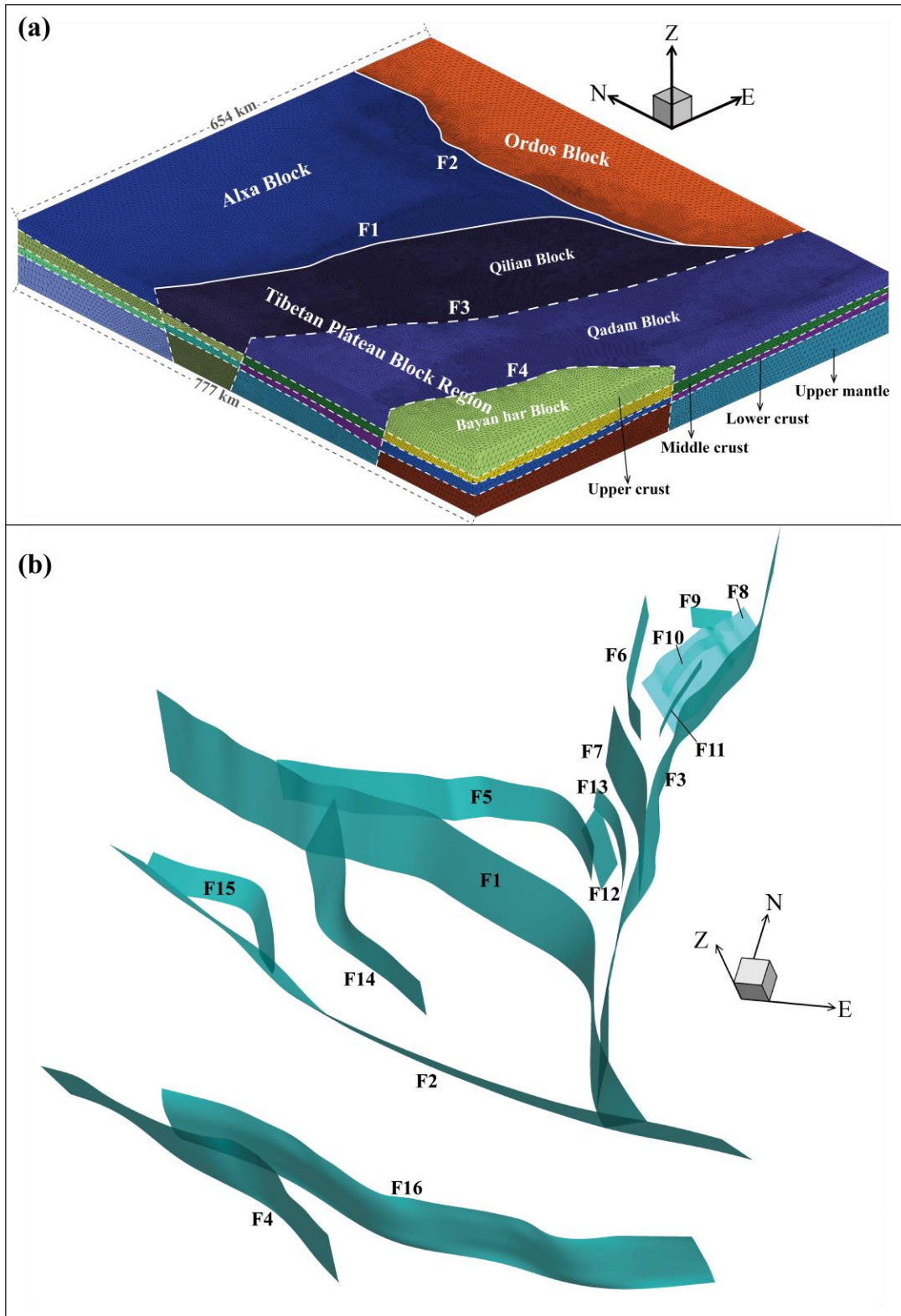
Figure 2. Model geometry and fault system. (a) Distribution of the rock types employed for the model. (b) Cyan surfaces indicate the faults implemented in the model as frictional contact surfaces. Fault names can be found in Fig. 1.

115

Table 1. Geometric parameters of faults in the model

	Fault name	Strike	Dip direction	Dip (°)	Reference
F1	/	NWW-SSE	SW	70	RGAFSAO, 1988
F2-1	ZZSF	N-S	W	70	Gao, 2020
F2-2	HHF	N-S	W	70	Bao et al., 2019
F2-3	LSF	N-S	W	80	Wang et al., 2013
F2-4	YWSF	N-S	W	70	NIGS, 2017
F2-5	XGSF	N-S	W	70	NIGS, 2017
F3-1	DTH-LXF	NWW-SSE	NE	70	Zhou et al., 2009
F3-2	WQLF				Li, 2005
F4-1	EKLF	NW-SE	NE	75	Z. Liu et al., 2017
F4-2	TZF				J. Li et al., 2019
F5	East TJSF	NW-SE	SW	70	RGAFSAO, 1988
	West TJSF	E-W	S	70	RGAFSAO, 1988
F6	WHLSF	N-S	W	80	Lei, 2015
F7	NSSF	NW-SE	SW	70	RGAFSAO, 1988
F8	EHLSF	NE-SW	SE	60	Du, 2010
F9	ZYGF	E-W	S	60	NIGS, 2017
F10	LHTF	NNE-SSW	SE	70	NIGS, 2017
F11	YCF	NNE-SSW	NW	70	NIGS, 2017
F12	YTSF	NW-SE	SW	65	NIGS, 2017
F13	QSHF	NW-SE	SW	45	Tian et al., 2020
F14-1	ZLHF	NNW-SSE	SW	45	Xu et al., 2016
F14-2	MXSF	NW-SE	SW	80	Hou et al., 1999
F15	LJSF	NWW-SSE	SW	50	Yuan et al., 2005
F16-1	DB-BLJF	NW-SE	SW	70	Yuan et al., 2007
F16-2	WD-KXF	E-W	SW	70	Jia et al., 2012

The detailed fault names are defined in Fig. 1.

Table 2. Rock properties of the finite element model

	Alxa Block			Ordos Block			Tibetan Plateau Block		
	E(Gpa)	ρ (g/cm^3)	ν	E(Gpa)	ρ (g/cm^3)	ν	E(Gpa)	ρ (g/cm^3)	ν
Upper crust	77.4	0.244	2.74	77.4	0.244	2.74	76.8	0.243	2.74
Middle crust	84.2	0.247	2.78	84.2	0.247	2.78	84.5	0.246	2.78
Lower crust	113.0	0.259	2.95	113.0	0.259	2.95	110.0	0.257	2.93
Upper mantle	194.0	0.278	3.39	191.0	0.278	3.37	187.0	0.278	3.36

E, ρ, and ν are Young's modulus, density, and Poison's ratio, respectively.
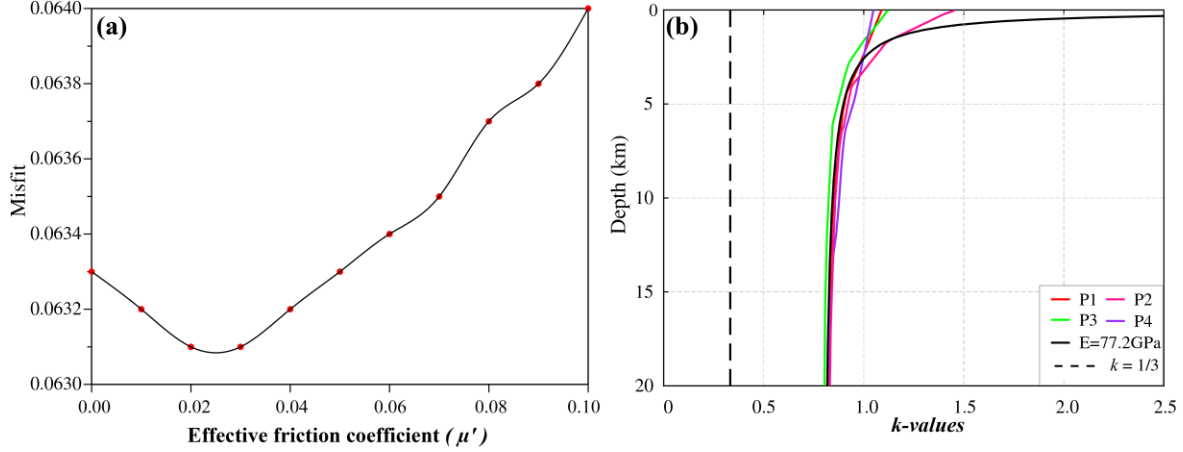
Figure 3. (a) Velocity misfit of the crustal velocity between the modeled results and GPS measurements as a function of the effective friction coefficient. The optimal friction coefficient was determined to be 0.02. (b) Depth profiles of the initial k-values at four test sites indicated in Fig. 1. The solid black line shows the stress state based on Equation (3), which was used as a reference stress state. For comparison, the low k-value based on the uniaxial strain state is also shown (dashed black line).

2.3 Friction coefficient

In our model, frictional faults were considered to obey the Mohr–Coulomb friction law:

$$\sigma_s = C_0 + \mu \cdot (\sigma_n - P_f) = C_0 + \mu' \cdot \sigma_n, \tag{1}$$

where σ_s is the shear stress on the fault surface at time of rupture, C_0 is the cohesion, μ is the coefficient of friction, σ_n is the normal stress on the fault surface, P_f is the pore pressure, and μ' is the effective coefficient of friction of the fault surface when accounting for the pore pressure. The cohesion C_0 of the rocks was assumed to be negligible (Jamison et al., 1980). The friction coefficient of the fault surface is important to the kinematics of a fault, but it is complex in a fault and varies in time and space. The exact magnitude of the friction coefficient can be affected by various external factors including fluid, temperature, stress states, and fault slip rate (Zhu et al., 2009). Therefore, it is challenging to obtain the precise friction coefficient of a fault. However, the results of many studies showed that large faults generally have low effective friction coefficients (Wang, 2021). For instance, the Haiyuan Fault has friction coefficients as low as 0.05 (He et al., 2013) and faults on the eastern margin of the TP have friction coefficients as low as 0.02 (Li et al., 2015; Li, Hergert, et al., 2021). Simulations were performed with a series of friction coefficients (0–0.1) and the results were compared with GPS observations (Cianetti et al., 2001). The results showed that setting a friction coefficient of 0.02 for all faults yields the smallest fitting error (Fig. 3a). To minimize the fitting error, localized adjustments were made for the friction coefficients of the F1 and F3 faults, which are large strike-slip faults. The final friction coefficients of F1, F3, and all other faults were 0.01, 0.1, and 0.02, respectively, with a fitting error of 0.0536.

2.4 Initial stress state

The crustal initial stress affects the state of stress acting on a fault, which further controls the kinematic of the fault via the Mohr–Coulomb friction law. Therefore, the selection of appropriate initial stress is important when studying fault slip rates based on geomechanics models. The initial stress state that is most commonly employed in previous

numerical modeling studies of the NETP is the uniaxial strain reference state (Zhu et al., 2016), which based on the boundary condition that no elongation occurs in the horizontal direction, and the strain only occurs in the vertical direction. In this stress state, the ratio (*k*) of mean horizontal stress to vertical stress is only dependent on the Poisson's ratio:

$$k = \frac{(S_H + S_h)}{2S_V} = \frac{v}{1-v},$$ (2)

where S_H, S_h, and S_V are the maximum horizontal, minimum horizontal, and vertical stress, respectively, and v is Poisson's ratio. For the typical v-value of 0.25, Equation (2) gives $k = 1/3$, which implies that the vertical stress acting on the rock mass far exceed the horizontal stress and that the crust is always in a normal faulting or extensional stress regime. However, this assumption contradicts the thrust and strike-slip stress regimes common in the crust. Furthermore, *k*-values obtained globally from *in situ* measurements always greatly exceed 1/3, even in extensional tectonic environments (Hergert and Heidbach, 2011).

Based on a spherical shell model, Sheorey (1994) proposed a method for the estimation of the initial crustal stress, which accounts for the curvature of the Earth, the properties of crustal and mantle materials, temperature fields, and other thermally dependent properties, as shown in Equation (3):

$$k = 0.25 + 7E \cdot \left(0.001 + \frac{1}{z}\right),$$ (3)

Where *E* is the Young's modulus (GPa); and *z* is the depth (m). Because the *k*-values predicted by this method are generally consistent with those obtained from the Continental Deep Drilling Program (Hergert and Heidbach, 2011), Equation (3) has been widely used in numerical modeling studies worldwide (Ahlers et al., 2021; Buchmann et al., 2007; Rajabi et al., 2017; Reiter et al., 2014; Hergert and Heidbach, 2011; X. Li et al., 2022). In this study, we used Equation (3) to calculate the initial stress state for our model. The exact procedure for obtaining the initial stress proposed by Sheorey (1994) has been described previously by Hergert (2009) in detail. Figure 3b shows that the modeled initial stress is in good agreement with the theoretical result given by Equation (3).

2.5 Kinematic boundary conditions

The lateral boundary conditions of our model were constrained by the GPS velocity field data of Wang and Shen (2020) and were assumed to be constant along depth (Wang et al., 2008). The top surface of the model was configured as a free boundary, whereas the bottom surface slid freely in the horizontal direction, with a vertical velocity of 0. The detailed boundary conditions are shown in Fig. 4. For the calculation, we used the finite-element software Abaqus^{TM} because its powerful nonlinear processing capabilities. The model time is set as 500 ka, which is required to generate a proper contemporary state of stress and deformation until the accumulated displacements at the boundaries are propagated into the model.
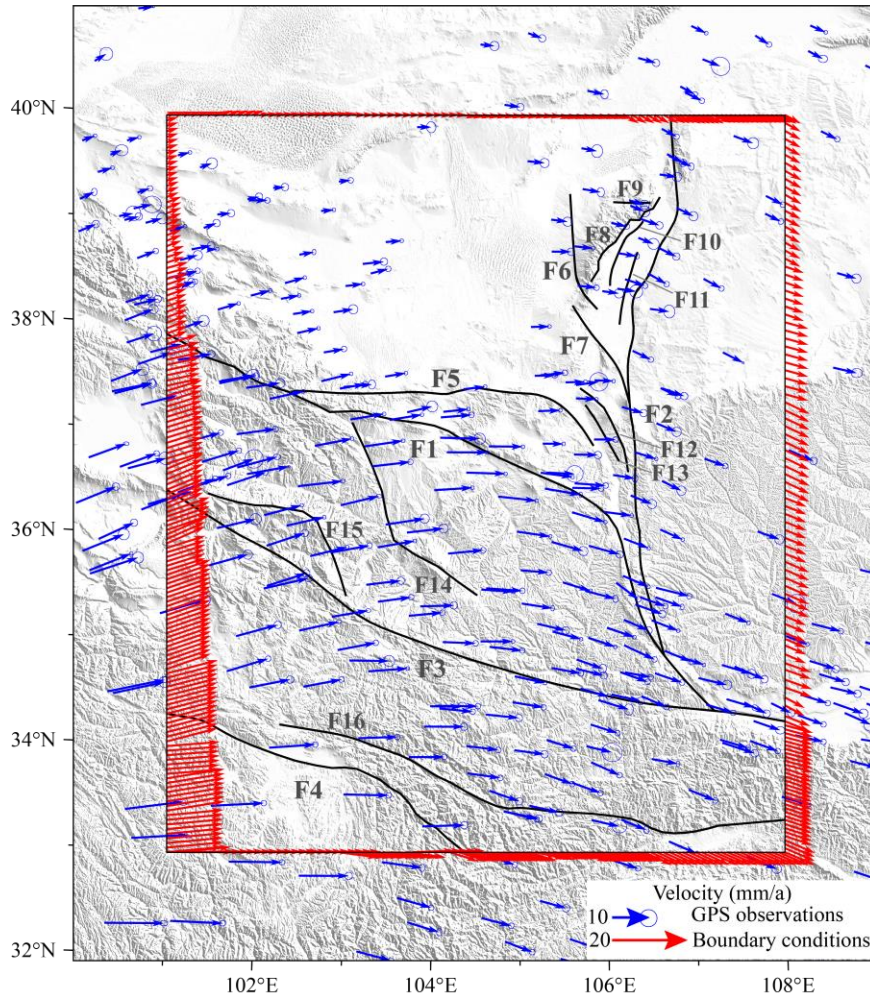
175

Figure 4. Boundary conditions of the model. The blue arrows represent the GPS observation velocities according to Wang and Shen (2020). The red arrows at the boundary represent the boundary velocities calculated by the interpolation of the GPS observations. Fault names can be found in Fig. 1.

3 Results

180   ### 3.1 Horizontal crustal velocities

The calculated horizontal crustal velocities in the study area are shown in Fig. 5. In terms of the direction, the western and central parts of the study area are moving in the NEE and near-EW directions and the eastern part gradually changes in motion toward the SW or SEE directions. Therefore, the study area is characterized by clockwise crustal motions. In terms of the movement rate, the model shows that the rates in the southwestern part of the study area are

185   high, whereas they are low in the northeastern part. The movement rates of the Alxa Block in the north and Ordos Block in the east are as low as ~4–6 mm/a. The Bayan Har Block in the south has the highest movement rate up to 13–14 mm/a. For the Qaidam Block and the Qilian Block, both of them exhibit a higher movement rate in the west than that in the east, decreasing from 12 to 9 and from 10 to 8, respectively.

In addition, Fig. 5 also shows that large strike-slip faults accommodate velocity gradients between adjacent blocks.

190   For example, the modeled velocity map can be divided in several parts by the F1, F3, and F4 block boundary faults,

across which the movement rates of the crust change remarkably, especially at the F1 fault. The movement rate on the southern side of the Qilian Block is 9–11 mm/a, whereas that on the northern side of the Alxa Block is 4–6 mm/a. A different rate of ≥3 mm/a between the two blocks is accommodated by the F1 fault.
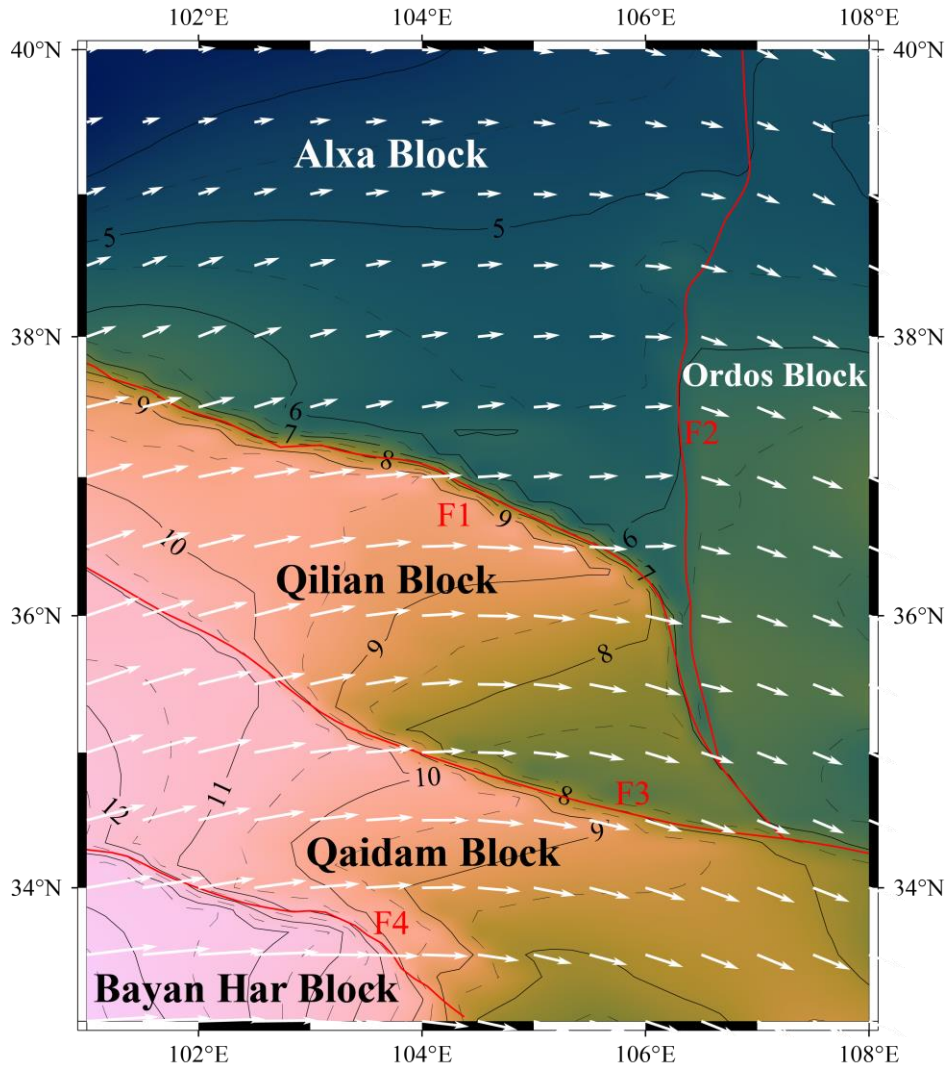
195 **Figure 5. Distribution of modeled crustal surface velocities of the NETP with a grid interval of 0.5° both in longitude and latitude. White arrows represent the crust movement direction. The background color contours represent the magnitude of the velocity in mm/a. The red lines represent the faults implemented in the model. The names are defined in Fig. 1.**
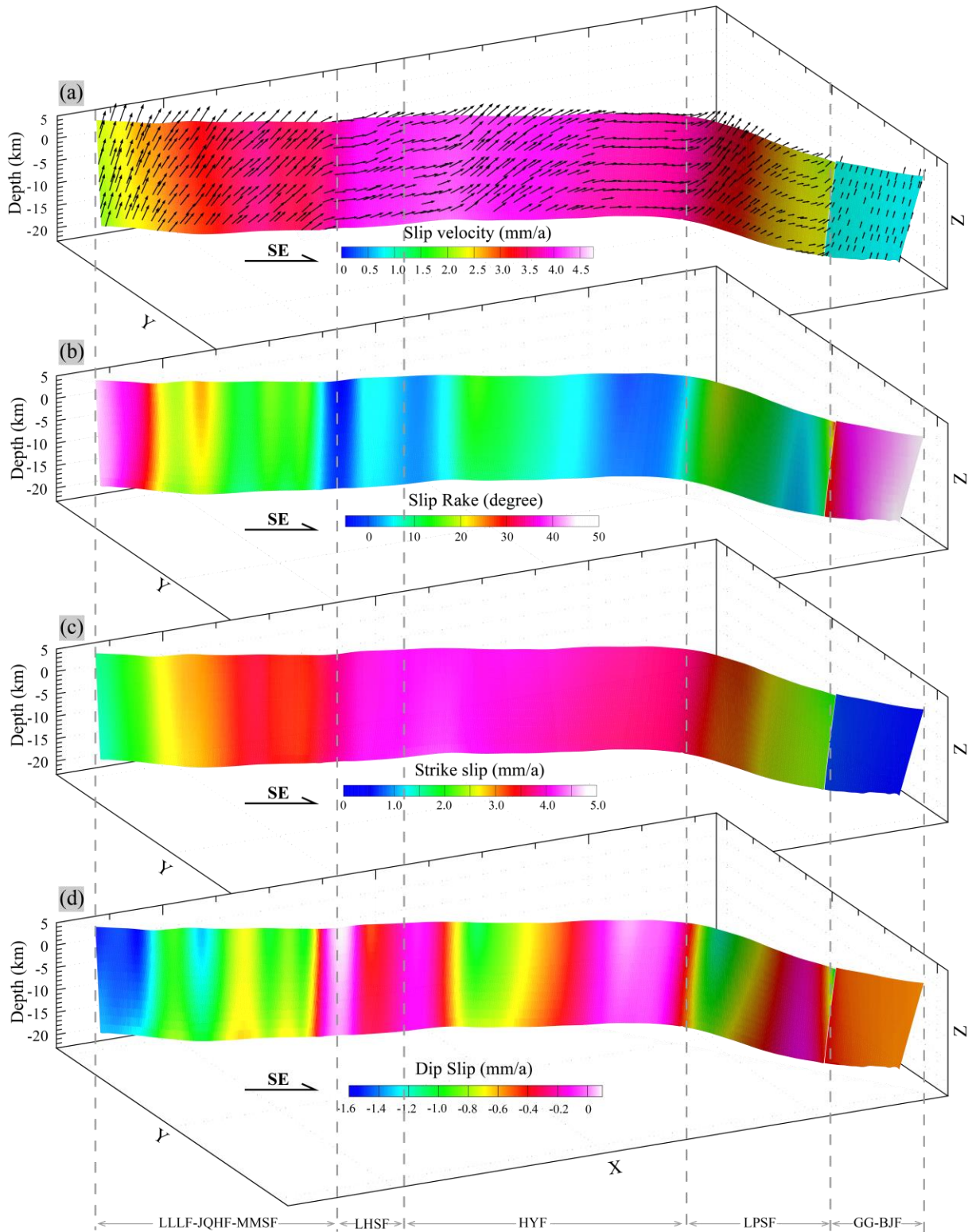
Figure 6. Distribution of the modeled fault slip rates on the F1 fault. View from NW to SE. The ratio of the vertical to horizontal scale is 4:1. (a) Total slip rates with slip directions (black arrows). Parts of the fault has an oblique-slip component. (b) Slip rake. Positive values indicate that the fault's movement has a thrust component. (c) Slip rates along the fault's strike. Positive values represent sinistral strike-slip. (d) Slip rates along the fault's dip direction. Negative values represent thrust faulting.

200

3.2 Fault slip rates of the main faults

205   The dominant depth range of seismic activities in the study area is 5–15 km, with a few events at depths up to 20 km (Li et al., 2020; Y. Li et al., 2021). As mentioned in the introduction, seismic activities are closely related to fault activities. In order to assess the seismic hazard reasonably on the faults in the NETP, we focused on the fault kinematics in the brittle crust and extracted the kinematic characteristics up to a depth of 20 km for the main faults from our 3D geomechanics model. The extracted kinematic characteristics are described below.

210   **3.2.1 Slip rate of the F1 fault**

From west to east, the F1 fault comprises the Lenglongling, Jinqianghe, Maomaoshan, Laohushan, Haiyuan, Liupanshan, and Guguan–Baoji faults (Fig. 1). Two earthquakes with magnitudes M ≥ 8.0 have occurred along this fault—the 1920 M 8.0 Haiyuan Earthquake and 1927 M 8.0 Gulang Earthquake, which formed 220 and 120 km long surface rupture zones, respectively (Guo et al., 2020; Liu-Zeng et al., 2015; Zhang et al., 1987). The kinematic state

215 of the F1 fault was extracted from the 3D geomechanics model, as shown in Fig. 6. On the western part of the F1 fault (Lenglongling, Jinqianghe, and Maomaoshan faults), the slip rates increase from 2.0 to 4.0 mm/a from west to east and continue to increase further east (Laohushan Fault and western part of the Haiyuan Fault) up to a maximum of 4.5 mm/a. The slip rates of the F1 fault decrease in the middle of the Haiyuan Fault. The eastern part of the Haiyuan Fault has a slip rate of ~3.5 mm/a. The slip rate of the Liupanshan Fault decreases in the SE direction and bottoms out at

220 ~2.0 mm/a; on the Guguan–Baoji Fault, the slip rate is lower than 1 mm/a (Fig. 6a). The slip rates obtained by our 3D geomechanics model for the Haiyuan Fault are much lower than earlier estimates (8.0–12 mm/a; Burchfiel et al., 1991; Lasserre et al., 1999; Zhang et al., 1988) but similar to more recent estimates (3.2–4.5 mm/a; Li et al., 2009; Matrau et al., 2019; Y. Li et al., 2017). The disagreements with earlier geological estimates may be related to the time scale and the extent to which faults have been studied (Li et al., 2009).

225   Although the F1 fault is predominantly a left-lateral strike-slip fault, it also has a thrust component (Fig. 6b). The Lenglongling, Jinqianghe, Maomaoshan, middle Haiyuan, and Liupanshan faults have the rake ranging from 10° to 20°, whereas the Guguan–Baoji Fault has the rake varying from 40° to 50°, indicating that they are oblique thrust faults. The Laohushan and western and eastern Haiyuan faults have rake below 10°, showing that left-lateral strike-slip faulting is dominant at these faults. Figures 6c and 6d show the continuous slip rates of the F1 fault along its strike

230 and dip, respectively. The slip rates along the strike (Fig. 6c) are like the total slip rates (Fig. 6a). The Laohushan and Haiyuan faults have the highest slip rates on the F1 fault. Conversely, the Lenglongling, Jinqianghe, Maomaoshan, and Liupanshan faults have high dip-slip rates.

3.2.2 Slip rate of the F2 fault

The F2 fault comprises the Zhuozishan, Huanghe, Luoshan, and Yunwushan–Xiaoguanshan faults (Fig. 1). Figure 7

235 shows that right-lateral strike-slip faulting is prevalent across the entire F2 fault. However, the magnitude of the dip-slip component varies from one location to another. The Zhuozishan Fault is an oblique-slip reverse fault with slip rates ranging from 0.8 to 1.6 mm/a. The Huanghe Fault has a slip rate of 1.6–2.6 mm/a. Its northern segment is an oblique-slip normal fault, whereas its southern segment has almost no dip-slip component. The Luoshan and
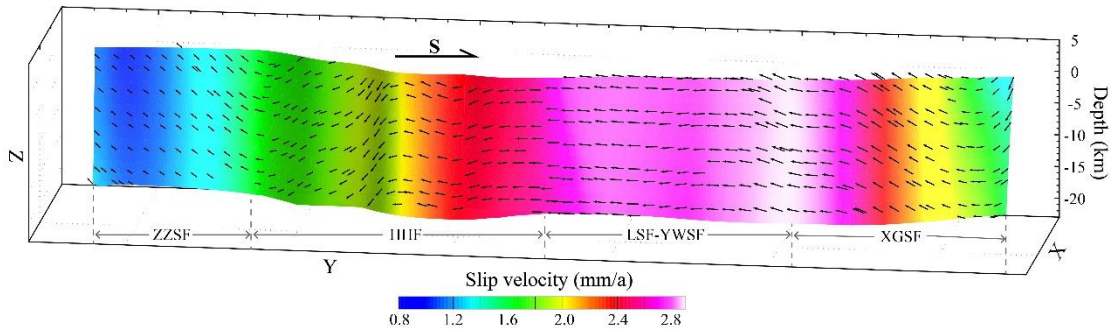
Figure 7. Distribution of the modeled fault slip rates on the F2 fault. View from west to east. The black arrows represent the slip directions. The ratio of the vertical to horizontal scale is 4:1.
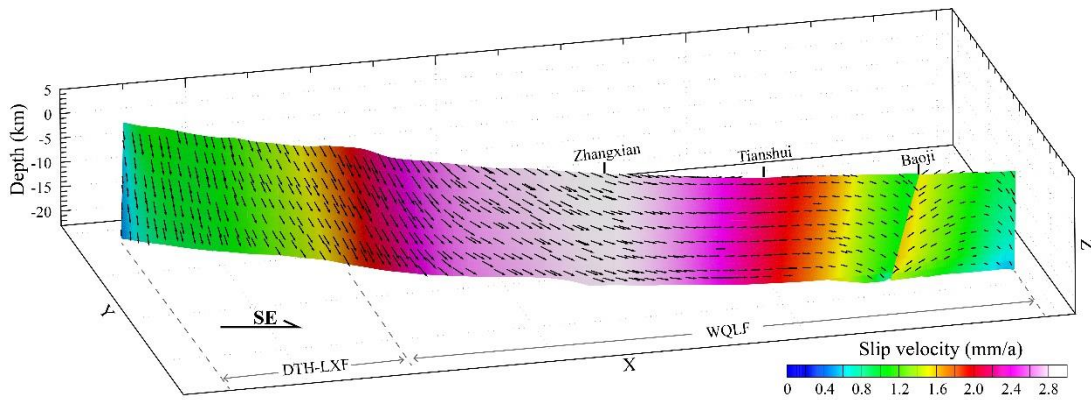
Figure 8. Distribution of the modeled fault slip rates on the F3 fault. View from SW to NE. The black arrows represent the slip directions. The ratio of the vertical to horizontal scale is 4:1.

Yunwushan faults have slip rates ranging from 2.6 to 3.0 mm/a and are dominated by right-lateral strike-slip faulting. The Xiaoguanshan Fault is an oblique-slip reverse fault with slip rates ranging from 3.0 mm/a (northern end) to 1.4 mm/a (southern end).

3.2.3 Slip rate of the F3 fault

The F3 fault includes the Daotanghe–Linxia and West Qinling faults (Fig. 1) and is mainly a left-lateral strike-slip fault, as shown in Fig. 8. The western Daotanghe–Linxia Fault is an oblique-slip reverse fault, which has slip rates ranging from 0.8 to 1.8 mm/a. The West Qinling Fault has slip rates varying from 1.8 to 2.8 mm/a, but each segment of this fault has slightly different kinematics. The West Qinling Fault is an oblique-slip reverse fault west of Zhangxian, but is dominated by left-lateral strike-slip faulting in the Zhangxian–Tianshui–Baoji region. The West Qinling Fault becomes an oblique-slip normal fault only in the vicinity of Baoji.

The kinematics of other faults in the study area are not described in this study. Their horizontal velocities are listed in Fig. 9.
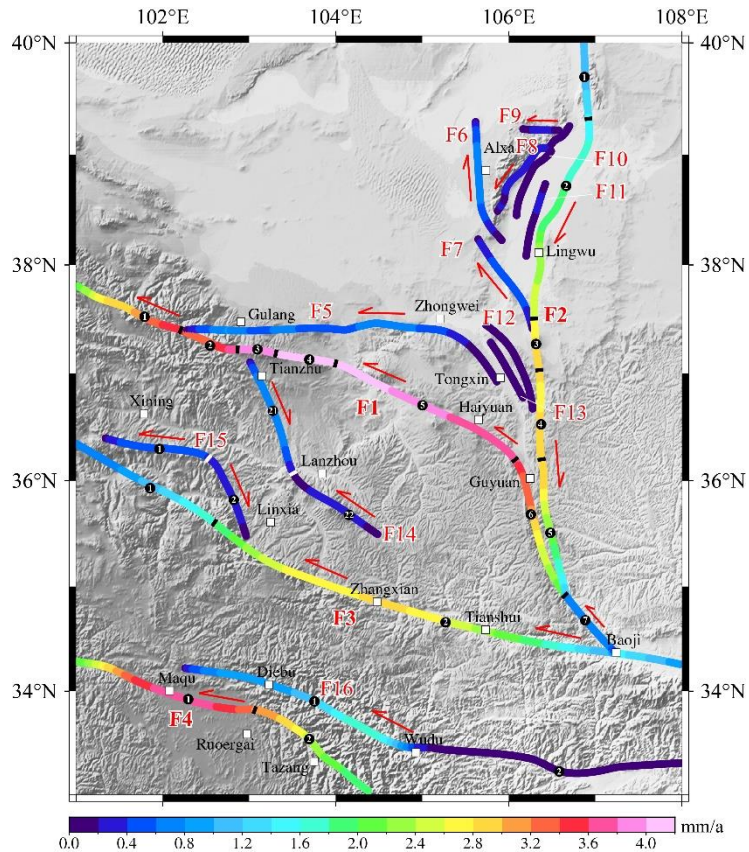
Figure 9. Modeled horizontal fault slip rates and slip senses. The fault names are defined in Fig. 1.

260
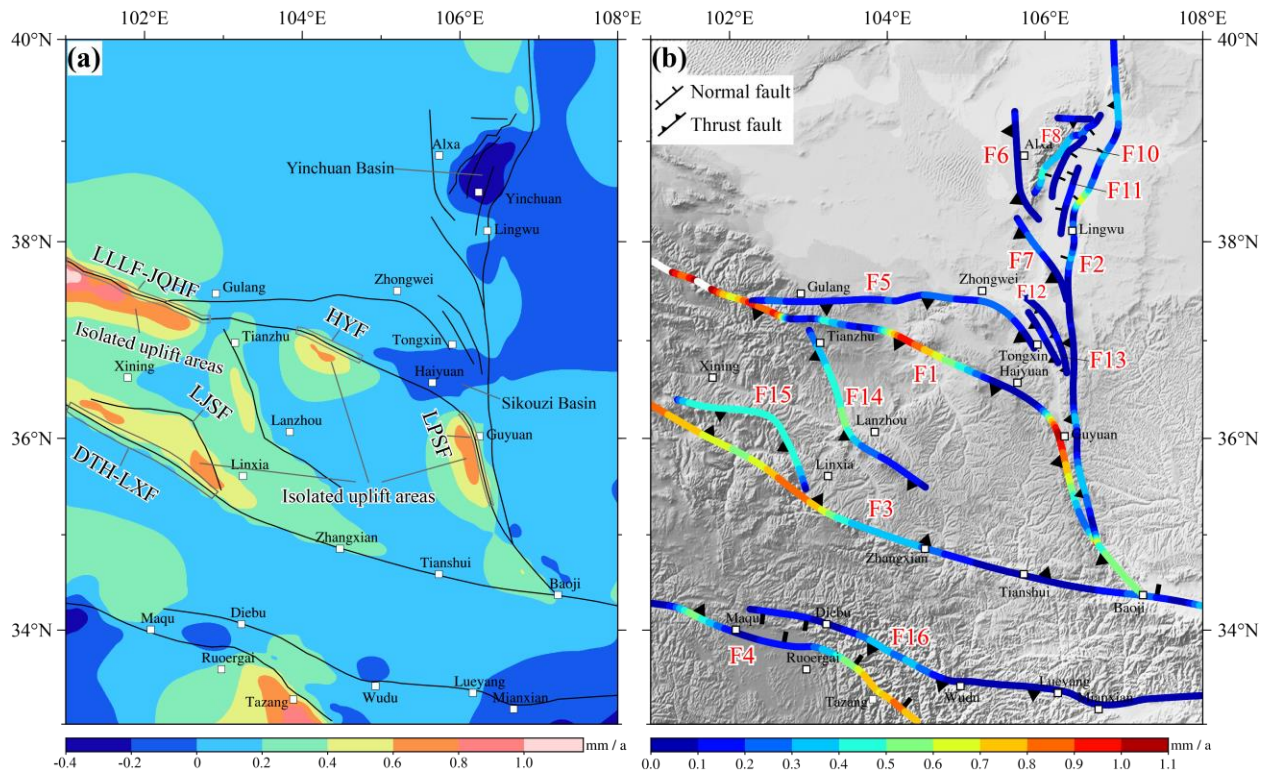
Figure 10. (a) Modeled vertical velocity at the surface. Negative values indicate subsidence, whereas positive values represent uplift. (b) Modeled vertical slip rates on faults at the surface. The fault names are defined in Fig. 1.

3.3 Vertical velocities

Figure 10a shows the distribution of vertical velocities in the study area. In our model, surface subsidence can be
265   observed only in the Yinchuan Basin west of Huanghe Fault, in the Ordos basin in the east, and in the Sikouzi Basin
in the southern Ningxia arc tectonic belt. Most of the subsidence rates range between 0 and 0.2 mm/a, except in the
center of the Yinchuan Basin, which exhibits subsidence rates varying from 0.2 to 0.4 mm/a. Based on paleomagnetic
studies, the Sikouzi Basin had a subsidence rate of 0.22 mm/a during the Pliocene (Wang et al., 2011), whereas the
subsidence rate of the Yinchuan Basin has been 0.32 mm/a since the Middle Pleistocene (Ma et al., 2021). Both values
270   are consistent with those derived from our simulation.

Most other parts of the study area exhibit uplifting, albeit at low rates (generally less than 0.2 mm/a). Most areas
with high uplift rates (0.8–1.0 mm/a) are in the Qilian Block such as the Lenglinglong Fault and Jinqianghe Fault, the
southern side of the middle Haiyuan Fault, the western side of the Liupanshan segment, and the southern side of the
Lajishan Fault (Fig. 10a). High vertical fault slip rates also appear on the F1 and F3 thrust faults that form the north
275   and south boundaries of the Qilian Block (Fig. 10b). These high vertical fault slip rates are inferred to be caused by
the compression from the NE expansion of the TP and SW subducting of the Alxa Block (Ye et al., 2015). Therefore,
outward thrust stacking occurs on the southern and northern boundaries (F1 and F3 faults) of the Qilian Block.

4 Discussion

4.1 Comparison with previous results

280   The boundary conditions of our model were derived from the GPS data of Wang and Shen (2020). Figure 11 shows a
comparison of the results of our model with the GPS data. The modeled velocity field is consistent in both direction
and magnitude with GPS-derived velocity field. In order to further examine the fit between the model results and GPS
data, we selected a NE–SW profile that crosses through the study area (Fig. 11, C–C') and projected all GPS-observed
values within 50 km of both sides of the profile. Figure 12 shows that the modeled and observed values on either end
285   of the profile (i.e., locations close to the model's boundaries) are almost identical. Although there were differences
between the modeled and GPS-observed values, the differences were within the margin of error for the GPS data.
Therefore, based on comparisons between the modeled and GPS-observed values in the map and profile, our modeled
kinematics agrees well with the GPS data.

Table 3 is a comparison of the modeled slip rates and model-independent geological slip rates compiled from
290   previous studies. From the comparison, we can see that our modeled results are generally consistent with the slip rates
obtained by geologic approaches. For example, the modeled horizontal slip rates on the F1 fault (e.g., the Laohushan,
Haiyuan, and Liupanshan faults) are similar to the geological slip rates obtained by previous pointwise measurements
(Table 3). The modeled slip rates on the F2-3 Luoshan Fault (2.6–3.0 mm/a) are in line with the geological slip rate
(2.2 mm/a). A good agreement between these two kinds of slip rates also exists on the West Qinling Fault in the
295   Zhangxian and Tianshui region (Table 3).
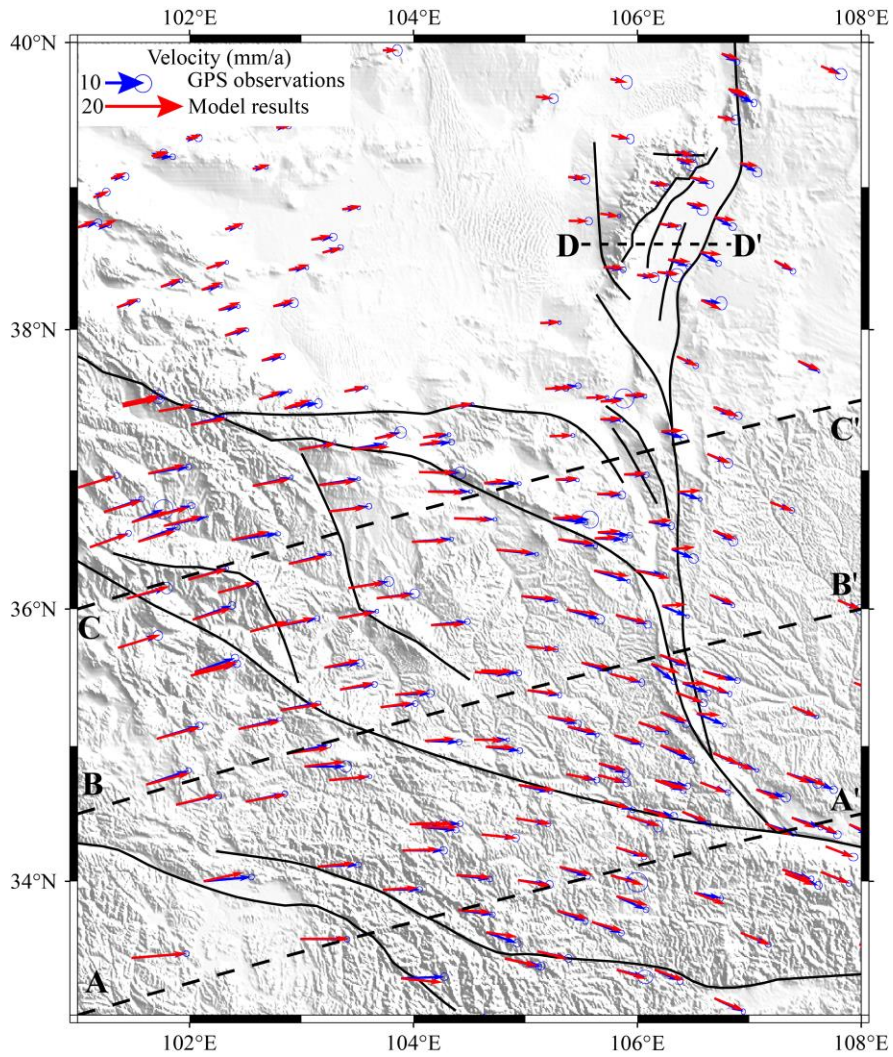
Figure 11. Comparison of the modeled horizontal velocities and GPS velocities. The red arrows represent the modeled results and the blue arrows are the GPS measurements (Wang and Shen, 2020). The dashed line is the location of the profile in Fig. 12 and Fig. 14.
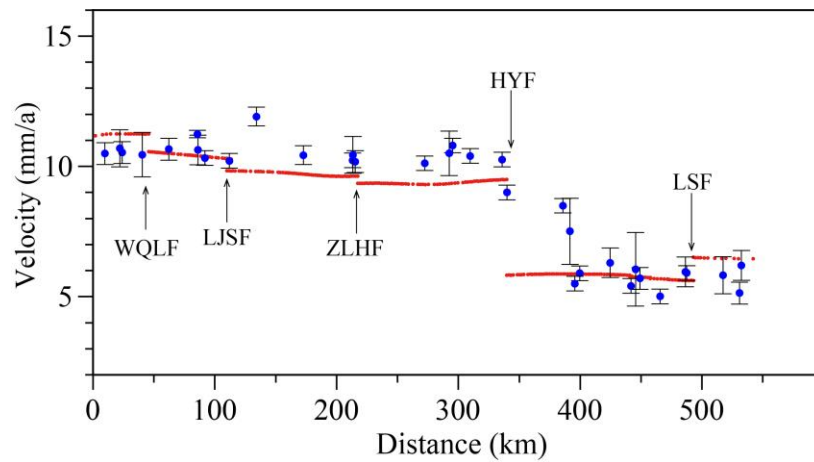
Figure 12. Comparison of the modeled horizontal velocities and GPS velocities along the C-C' profile in Fig. 11. The red points are model data and blue circles indicate GPS measurements. The fault names are defined in Fig. 1.

Table 3. Comparison of model slip rates with geological slip rates

Fault name		Modeled rate (mm/a)		Geological rate (mm/a)		References
		Lateral [a]	Vertical [b]	Lateral [a]	Vertical [b]	
F1-1	LLLF	2.8–3.6	0.6–1.3	3.9	0.38	He et al., 2000, 2010
F1-2	JQHF	3.2–3.8	0.7–1.0	4.4	/	He et al., 2000
F1-3	MMSF	3.8–4.0	/	3.7	/	He et al., 2000
F1-4	LHSF	4.0–4.2	/	4.0	/	Liu et al., 2018
F1-5	HYF	3.6–4.2	0.2–1.0	3.2–4.5	/	Li et al., 2009; Matrau et al., 2019
F1-6	LPSF	2.0–3.6	0.2–1.1	0.7–3.0	0.2–0.9	Wang, 2018; Wang et al., 2021;
F1-7	GG-BJF	0.6–0.8	0.5–0.6	/	/	/
F2-1	ZZSF	- (1.2–1.4)	0.2–0.3	/	/	/
F2-2	HHF	- (1.6–2.6)	0–0.7	/	0.04–0.24	Lei et al., 2014
F2-3	LSF	- (2.6–3.0)	/	- 2.2	/	Min et al., 2003
F2-4	YWSF	- (2.6–3.0)	/	/	/	/
F2-5	XGSF	- (1.4–3.0)	0–0.4	/	/	/
F3-1	DTH-LXF	0.8–1.8	0.5–0.8	/	/	/
F3-2	WQLF	2.0–3.0	0.1–0.9	2.5–2.9	/	Chen et al., 2019
F4-1	EKLF	3.2–3.8	0–0.5	4.9	0.25	Li, 2009
F4-2	TZF	2.2–3.2	0.3–0.7	1.4–3.2	0.1–0.3	Ren et al., 2013
F5	TJSF	0–0.8	0.1–0.3	0.77–0.96	0.1–0.2	X. Li et al., 2017, 2019; Zhang et al., 2015
F6	WHLSF	- (0.6–0.8)	0–0.2	- 0.28	0.11	Lei, 2016
F7	NSSF	- (0.4–0.6)	0–0.3	- 0.35	0.10	Lei, 2016
F8	EHLSF	0.2–0.4	0.1–0.5	/	0.88	Lei et al., 2016
F9	ZYGF	0.2–0.4	0–0.2	/	/	/
F10	LHTF	/	0–0.1	/	0.18	Lei et al., 2011
F11	YCF	/	0–0.2	/	0.14	Lei et al., 2008
F12	QSHF	/	0–0.2	/	/	/
F13	YTSF	/	0–0.2	/	/	/
F14-1	ZLHF	- (0.6–0.8)	0.2–0.6	/	0.12–0.51	Hou et al., 1999
F14-2	MXSF	0.2–0.4	0.1–0.4	0.5–1.72	/	Song et al., 2006
F15-1	WLJSF	0.4–0.6	0.4–0.5	/	/	/
F15-2	ELJSF	- (0.2–0.4)	0.3–0.5	/	/	/
F16-1	DB-BLJF	0.8–1.8	0.1–0.4	1.3	0.39	Liu et al., 2015
F16-2	WD-KXF	0–0.2	0-0.1	1.0	/	Zheng et al., 2016a

[a] Positive value indicates left-lateral slip rate. [b] Fault attributes are shown in Fig. 10b

4.2 Fault slip rates and seismic hazards

4.2.1 Tianzhu Seismic Gap

The M 8.0 Gulang earthquake occurred in 1927 in the northwestern part of the F1 fault, whereas the M 8.0 Haiyuan earthquake occurred in 1920 on the Haiyuan Fault (Fig. 1). The Jinqianghe, Maomaoshan, and Laohushan faults, which are in the region between the locations of these two strong earthquakes, unruptured in the two earthquakes, are collectively known as the Tianzhu Seismic Gap (TSG, Guo et al., 2019; Li et al., 2016; Fig. 13a). Based on the simulation, the left-lateral strike-slip rates of the Jinqianghe, Maomaoshan, and Laohushan faults were 3.2–3.8, 3.8–4.0, and 4.0–4.2 mm/a, respectively (Table 2, Fig. 13a). Therefore, all three faults have relatively high slip rates compared with the rest of the study area. Based on the slip rates and other fault data, we estimated the earthquake magnitude based on the energy accumulated during the time elapsed from the previous event (Purcaru et al., 1978) and recurrence intervals (Shen et al., 2009), as shown in Table 4. The Jinqianghe, Maomaoshan, and Laohushan faults can generate M_S 7.1, M_S 7.3, and M_S 6.6 earthquakes, with recurrence intervals of 424, 571, and 1910 years, respectively. It has been reported that 675 and 952 years have elapsed since the last time Jinqianghe and Maomaoshan faults ruptured (Gan et al., 2002; Table 4). Therefore, the likelihood these two faults will reactivate is high. For the Laohushan Fault, it is believed that the most recent earthquake with surface ruptures was the 1888 M 6.25 Jingtai earthquake. Because only 133 years have elapsed since this event, the seismic hazard of this fault in the near future is low. Although several researchers suggested that the TSG could be ruptured thoroughly by a M ≥ 8.0 earthquake with a recurrence interval of 1000 years (Chen, 2014) and the elapsed time from the last M 8.0 earthquake may be closed to the recurrence interval (Liu et al., 2018), further work is needed to verify this assumption, especially on the stress state of the faults. Nevertheless, our results together with the previous studies suggest that the seismic hazard caused by a large earthquake in the TSG is high in the next few decades, careful earthquake monitoring should be conducted in this area.

4.2.2 Seismic gap at the southern Liupanshan and Guguan–Baoji faults

The Liupanshan and Guguan–Baoji faults are jointly affected by three interacting blocks with contrasting velocity fields (Fig. 13b). First, the SE movement of the Qilian Block horizontally compresses this region against the stable Ordos Block to the east and causes strong thrusting motion (Fig. 6a). Second, the Liupanshan Fault zone, which is adjacent to the SE end of the Haiyuan Fault, accommodates the shortening caused by the left-lateral strike-slip motion of the Haiyuan Fault. Third, our modeled results show that the Yunwushan–Xiaoguanshan Fault has a significant right-lateral strike-slip component (Fig. 7), which contributes to the accumulation of right-lateral shear strain in the Liupanshan and Guguan–Baoji fault zones (Du et al., 2018). Based on the analysis of the velocity field in the region, the Liupanshan and Guguan–Baoji faults are prime location for elastic strain accumulation. The distribution of the velocities of the faults are also indicative of stress accumulation in this region (Fig. 7). The northern segment of the Liupanshan Fault has slip rates of 3.2–3.6 mm/a, which dramatically decrease to 2.5 mm/a in the middle and southern segments of the fault. In addition, the slip rate of the Guguan–Baoji Fault is only 0.7 mm/a. The northern part of the Yunwushan-Xiaoguanshan Fault has slip rates of 2.8–3.0 mm/a, which decrease to 1.5 mm/a in the southern part (Fig. 13b). These changes in the slip rate indicate that the middle–southern segments of the Liupanshan and Guguan–Baoji
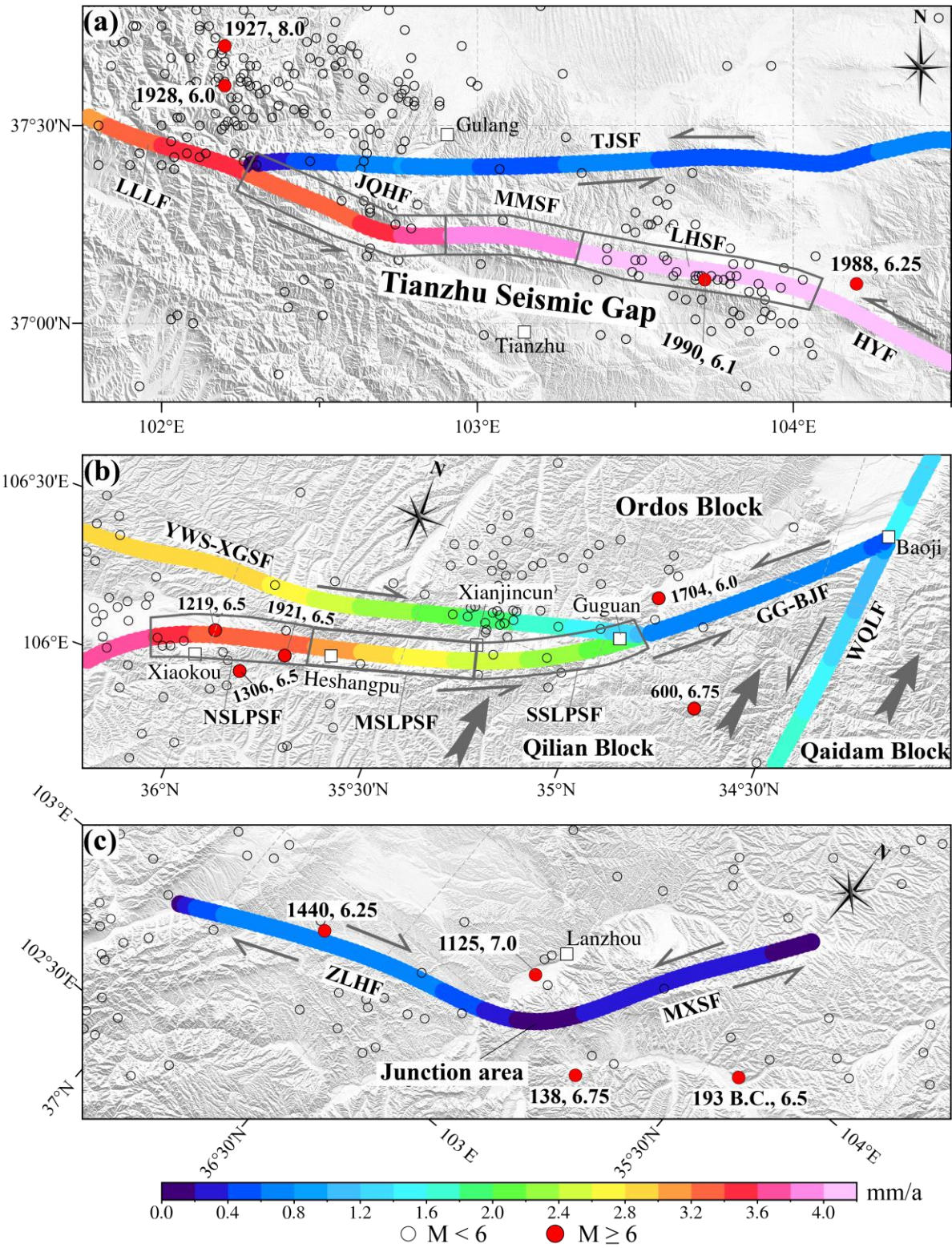
Figure 13. Modeled horizontal fault slip rates and distribution of historical earthquakes in (a) the Tianzhu Seismic Gap, (b) the intersection area of the Liupanshan, Guguan–Baoji, and Yunwushan–Xiaoguanshan faults and (c) the junction area of the Maxianshan and Zhuanglanghe faults. The gray arrows in (b) represent the movements of the Qilian and Qaidam blocks and NSLPSF, MSLPSF, and SSLPSF are the northern, middle, and southern segments of the Liupanshan Fault, respectively.

345

Table 4. Earthquake magnitude and recurrence interval of each fault based on the energy accumulated during the elapsed time since the last remarkable earthquake

Fault name	V_1(mm/a)	V_2(mm/a)	L_1 (km)	L_2 (km)	μ (Gpa)	t	S (m)	M_S	T (a)
JQHF	3.5	/	34	20	34.5	675	1.5	7.1	424
MMSF	3.9	/	51	20	34.5	952	2.2	7.3	571
LHSF	4.1	2.5	70	20	34.5	133	3.1	6.6	1910
MSLPSF, SSLPSF	2.5	/	80	23	34.5	570	3.5	7.2	1397
GG-BJF	0.7	/	70	23	34.5	1400	3.1	7.1	4365

V_1 is the modeled average slip rate of the fault in this study; V_2 is the aseismic creep rate of the fault (Y. Li, et al., 2021); L_1 is the length of the fault (Xu et al., 2016); L_2 is the depth of the seismogenic, which refers to the locking depth (Y. Li, et al., 2017, 2021); μ is the shear modulus of the rocks (Aki et al., 2002); t is the time that has elapsed since the most recent remarkable earthquake (Gan et al., 2002; Shi et al., 2013, 2014; Wang et al., 2001); S is the largest maximum coseismic displacement, calculated using the method of Gan et al. (2002); M_S is the earthquake magnitude corresponding to the energy accumulated by the fault between recurrences (Purcaru et al., 1978); T is the recurrence interval of the fault, where T = S/(V_1-V_2) (Shen et al., 2009). The fault names are defined in Fig. 1 and Fig. 13.

faults have high slip rate deficits, implying this region accumulates strain. However, in terms of seismic activity, only the northern part of the Liupanshan Fault has a history of major earthquakes including an M 7 earthquake in 1219, M 6.5 earthquake in 1306, and M 6.5 earthquake in 1921 (Fig. 13b). Earthquakes stronger than M 6.0 have not been recorded in the middle–southern parts of Liupanshan Fault. Their seismic activity mainly manifests as small and sparse earthquakes and the most recent remarkable activation was recorded ~570 years ago (Shi et al., 2014). Minor earthquakes related to the Guguan–Baoji Fault are scarce and the only notable earthquakes that have occurred near this fault are an M6.0 earthquake in 1704 and the 600 AD Qinlong M 6.75 earthquake (Shi et al., 2013). It has been estimated that ~1400 years have elapsed since the last M~7 earthquake.

Base on the above analysis, we suggest that the southern segments of the Liupanshan and Guguan–Baoji faults are in prime locations for stress/strain accumulation and constitute a seismic gap at the end of the large-scale Haiyuan strike-slip fault zone. Since this region has a history of strong earthquakes, it is necessary to assess the seismic hazard and its urgency in this region. Based on the fault slip rates obtained from our model and fault data in the literature, we estimated that the energy accumulated on the middle–southern Liupanshan and Guguan–Baoji faults during the elapsed time is sufficient to generate M_S 7.2 and M_S 7.1 earthquakes, with recurrence intervals of 1397 and 4365 years, respectively (Table 4). Obviously, the elapsed time on the middle–southern Liupanshan (570 years) and Guguan–Baoji faults (1400 years) (see the column "t" in Table 4) are much shorter than their typical recurrence intervals. Therefore, we infer that the middle-southern Liupanshan fault and the Guguan-Baoji fault are most likely in a state of stress accumulation, and the likelihood of a large earthquake on these fault segments in the next few decades is thought to be low.

4.2.3 Maxianshan–Zhanglanghe fault zone

The Maxianshan Fault near Lanzhou city is a large Holocene strike-slip fault with a component of thrusting and acts as an important earthquake-controlling fault that affects and constrains the seismicity of this region (Yuan et al., 2003). Different left-lateral strike-slip rates have been reported for this fault—3.73 mm/a (Yuan et al., 2002a), 0.5–1.72 mm/a

370   (Song et al., 2006), and 0.93 mm/a (Liang et al., 2008). These discrepancies in fault slip rate may be attributed to the loess that covers the extension of the fault, which obscures the fault traces in many segments and makes it difficult to track its activity. The modeled results in this study indicate that the left-lateral strike-slip rates of the Maxianshan Fault range from 0.2 to 0.4 mm/a and that the vertical slip rates vary from 0.1 to 0.4 mm/a (Fig. 13c, Table 3). Therefore, the left-lateral strike-slip rates of the Maxianshan Fault may not be as large as previously thought, but they have a

375   relatively large thrust component. The Zhanglanghe Fault is predominantly a right-lateral strike-slip fault with slip rates ranging from 0.6 to 0.8 mm/a (Fig. 13c, Table 3). These slip rates are significantly greater than the left-lateral strike-slip rates of the Maxianshan Fault. Note that the slip rate on the junction between the Maxianshan fault and Zhuanglanghe fault is almost zero. It can be inferred that the junction area would accumulate high concentrations of stress under the continuous eastward movement of the Qilian Block. Some have suggested that the 1125 Lanzhou M

380   7.0 earthquake occurred in such a tectonic setting (He et al., 1997; Fig. 13c). Given that the recurrence interval of this region is 2250–3590 years and the last event was only 896 years ago (Liang et al., 2008), the near-term risk of a large earthquake in this region is low. Therefore, we speculate that the junction area of the Maxianshan fault and Zhuanglanghe fault is currently in a state of stress accumulation.

4.2.4 Isolated uplift areas and earthquakes

385   As mentioned above, we considered that earthquakes are less likely to occur on the Laohushan, Liupanshan and Haiyuan faults in the short term from the perspective of the earthquake recurrence cycle and the elapsed from the previous earthquake. However, the Haiyuan, Liupanshan, Lajishan and Daotanghe-Linxia faults are all located near the isolated rapid uplift areas of Qilian block (Fig. 10a). Many studies have also found that low-velocity bodies are widely distributed in the middle-lower crust of the Qilian block (Bao et al., 2013; Wang et al., 2018; Ye et al., 2016).

390   The spatial coupling of active faults, isolated uplift areas and low-velocity bodies is highly similar to the seismogenic conditions elaborated by the "seismic source cavity" model recently proposed by Zeng et al. (2021). That is, during the rapid uplift of the isolated areas (Fig. 10a), the low-velocity bodies in the middle-lower crust easily intruded into the weak space of the crust under the action of differential pressure to form a "seismic source cavity". If the isolated uplift areas keep to rise, the "seismic source cavity" may rise to the shallow part of the crust to intersect with brittle

395   faults, causing strong earthquakes (Yang et al.,2009; Zeng et al., 2021). Therefore, in addition to the Jinqianghe and Maomaoshan faults mentioned above, the Haiyuan fault, Liupanshan fault, Lajishan fault and the Daotanghe-Linxia fault also have favorable structural conditions for strong earthquakes although some areas have not experienced in history.

4.3 Implication for deformation mechanism of NETP

400   The deformation of NETP is the result of the combined action of block rotation, faulting, and the intrablock straining (Meade and Loveless, 2009). We analyzed four velocity profiles to compare the contributions of block rotation, faulting, and intrablock straining to the total deformation of NETP (Fig. 14). It is noted that the rigid displacements caused by block rotation were calculated according to the Euler pole locations and rotation rates with respect to the Eurasia plate (Wang et al., 2017; Y. Li et al., 2022), as shown in Fig. 14 a–d. The velocity gradient caused by block

405 rotation accounts for more than 80% of that on the profiles. Obviously, the block rotation should be the primary mechanism for the deformation of the NETP, which is similar to the southeastern Tibet (Z. Zhang et al., 2013). However, the intrablock straining of Bayan Har and Qaidam blocks contribute approximately 4 mm/a and 3 mm/a shortening in profiles of AA', BB' (Fig. 14a–b). The Qilian block also has a contribution of 2 mm/a shortening in profile BB' but decreases to about 1mm/a in profile CC' (Fig. 14b–c). Therefore, the intrablock straining is still

410 significant for regional deformation. The boundary faults of the blocks, such as the East Kunlun fault, Haiyuan fault, West Qinling fault, also play an important role in regulating the deformation differences between blocks.

The D–D' profile shows that the tectonic deformations of the Yinchuan Basin structural belt slightly differ from those in other profiles. The NE expansion of the TP leads to near-N–S compression on the Yinchuan Basin (Yang, 2018), which causes it to move eastwards faster than the Alxa Block. This manifests as an eastward extension in the

415 Yinchuan Basin. The crustal deformations caused by this process are accommodated by the right-lateral strike-slip of Huanghe Fault (Fig. 14d).
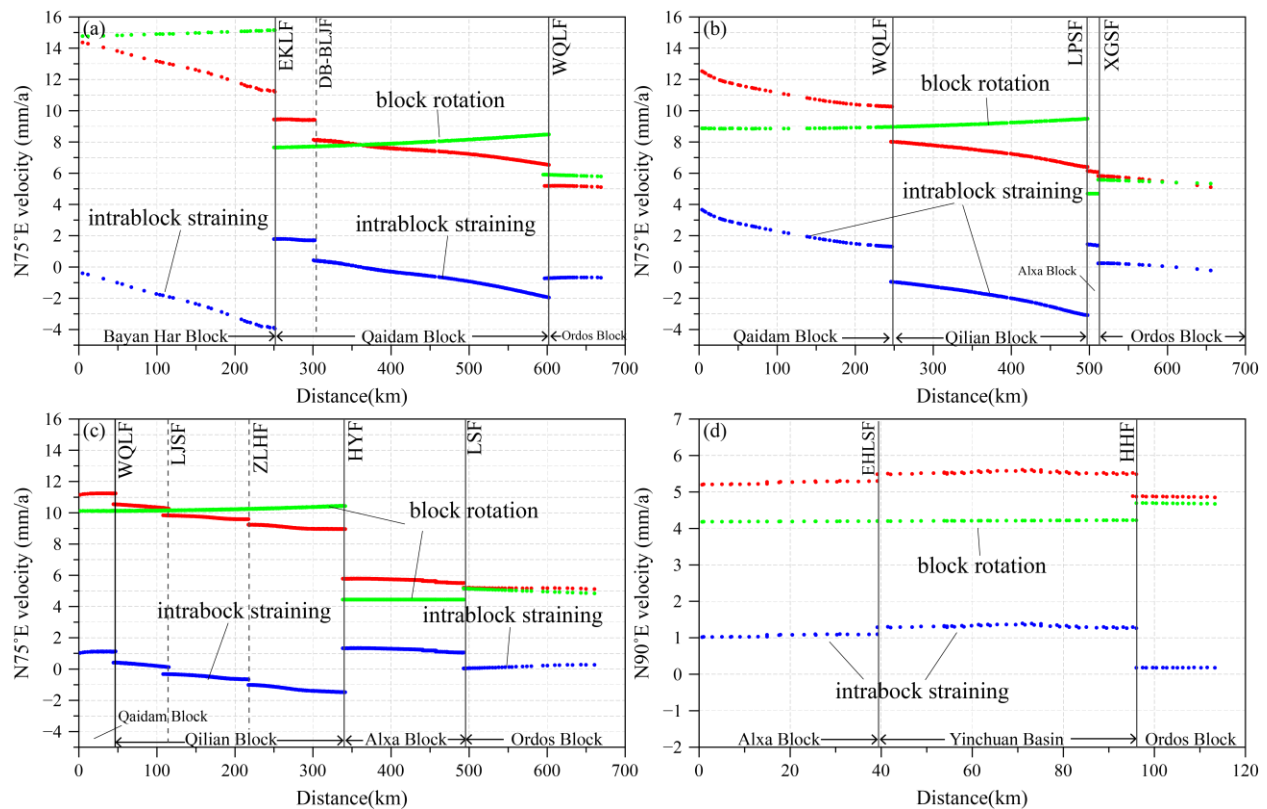
Figure 14. Modeled velocity profiles across the study area with orientation of profiles. The profiles in (a)–(d) correspond to the AA', BB', CC', and DD' in Fig. 11, respectively. The red dots indicate the components along the profiles of the node
420 **motion velocity within 2 km on both sides of the profile. The green dots represent the velocity component along the profiles due to plate rotation. The blue dots indicate the differences between the red and green dots. Fault names are defined in Fig. 1.**

5 Conclusions

In this study, a detailed 3D geomechanical model of the NETP was constructed based on geophysical, geodetic, and
425 geological data. This model accounts for 3D fault geometries, variational rock properties, a reasonable initial crustal

stress, and gravity. Special attention has been paid to the evaluation of fault friction coefficients and initial stress to ensure that the model is consistent with the real geological conditions as much as possible. After that, we extracted particular data from the model and obtained the horizontal and vertical crustal velocities of the study area as well as the horizontal and vertical slip rates of the major faults. The results can be mutually confirmed with the conclusions obtained by geodesy, geology, paleomagnetism, etc.

430

Based on the analysis of the kinematics of major faults, we suggest that the Jinqianghe–Maomaoshan Fault will probably cause a M_S 7.1–7.3 earthquake in the following decades due to its relatively high slip rates with an elapsed time close to the recurrence interval. In contrast, the Laohushan and middle–southern Liupanshan faults as well as the Guguan–Baoji and the junction area of the Maxianshan and Zhuanglanghe faults are inferred to have a low seismic hazard in the near future on account of their very short elapsed time, although stress is easily accumulated in these areas. The model also provided information on the deformation mechanism of the NETP. Because of velocity differences between the opposing sides of the Haiyuan, West Qinling, and East Kunlun faults, as well as the relative stability of the Alxa and Ordos blocks, the NE expansion of the TP has caused the fault-separated Qilian, Qaidam, and Bayan Har blocks to extrude in the SEE direction and rotate in the clockwise direction. The block rotation is the primary mechanism for the deformation of the NETP even though the intrablock straining and faulting are non-negligible.

435

440

Data Availability

The GPS data displayed in Fig. 4 and Fig. 11 are available through Wang and Shen (2020). The fault traces were obtained from Xu et al. (2016). The CRUST1.0 was obtained from Laske et al. (2013).

445 **Author contribution**

LL and XL contributed to the model building. LL carried out the analysis, wrote the paper, and prepared the figures. FY, LP and JT reviewed and edited the paper.

Competing interests

The authors have no competing interests to declare.

450 **Disclaimer**

Publisher's note: Copernicus Publications remains neutral with regard to jurisdictional claims in published maps and institutional affiliations.

Acknowledgments

This research was funded by the Ningxia Natural Science Foundation (Grant numbers: 2020AAC03445, 2021AAC05022 and 2021AAC03441). Some figures were plotted using The Generic Mapping Tools (https://www.generic-mapping-tools.org/). Slip rates on fault surfaces were calculated by the software GeoStress (Stromeyer et al., 2020).

References

Ahlers S., Henk A., Hergert T., Reiter K., Müller, B., Röckel, L., Heidbach, O., Morawietz, S., Scheck-Wenderoth, M., and Anikiev, D.: 3D crustal stress state of Germany according to a data-calibrated geomechanical model, Solid Earth, 12, 1777–1799, https://doi.org/10.5194/se-12-1777-2021, 2021.

Aki, K. and Richards, P.G.: Quantitative Seismology, second ed, University Science Books, California, USA, 2002.

Armijo R., Flerit F., King G., and Meyer B.: Linear elastic fracture mechanics explains the past and present evolution of the Aegean, Earth Planet Sc. Lett., 217, 85–95, https://doi.org/10.1016/S0012-821X(03)00590-9, 2004.

Bai M., Chevalier M., Pan J., Replumaz A., Leloup P. H., Métois M., and Li H.: Southeastward increase of the late Quaternary slip-rate of the Xianshuihe fault, eastern Tibet. Geodynamic and seismic hazard implications, Earth Planet. Sc. Lett., 485, 19–31, https://doi.org/10.1016/j.epsl.2017.12.045, 2018.

Bao G., Chen H., Hu J., and Zhu G.: Quaternary Activity and Segmentation of the Yellow River Fault of the Eastern Margin of Yinchuan Graben, Acta Geoscientica Sinica, 40, 614–628, 2019.

Bao X., Song X., Xu M., Wang L., Sun X., Mi N., Yu D., and Li H.: Crust and upper mantle structure of the North China Craton and the NE Tibetan Plateau and its tectonic implications, Earth Planet. Sc. Lett., 369–370, 129–137, https://doi.org/10.1016/j.epsl.2013.03.015, 2013.

Brotons V., Tomas R., Ivorra S., Grediaga A., Martı´nez-Martı´nez J., Benavente D., and Go´mez-Heras M.: Improved correlation between the static and dynamic elastic modulus of different types of rocks, Mater. Struct., 49, 3021–3037, 2016.

Buchmann T. J., and Connolly P. T.: Contemporary kinematics of the Upper Rhine Graben: A 3D finite element approach, Global Planet. Change, 58, 287–309, https://doi.org/10.1016/j.gloplacha.2007.02.012, 2007.

Burchfiel, B. C., Zhang P., Wang Y., Zhang W., Song F., Deng Q., Molnar P., and Royden L.: Geology of the Haiyuan Fault Zone, Ningxia-Hui Autonomous Region, China, and its relation to the evolution of the Northeastern Margin of the Tibetan Plateau, Tectonics, 10, 1091–1110, https://doi.org/10.1029/90TC02685,1991.

Chen P., and Lin A.: Tectonic topography and Late Pleistocene activity of the West Qinling Fault, northeastern Tibetan Plateau, J. Asian Earth Sci., 176, 68–78, https://doi.org/10.1016/j.jseaes.2019.02.007, 2019.

Chen T.: Application of airborne LiDAR (light detection and ranging) for quantitative tectonic geomorphology, PH.D. thesis, Institute of Geology China Earthauake Administration, Beijing, 2014.

Cianetti S., Gasperini P., Giunchi C., and Boschi E.: Numerical modelling of the Aegean-Anatolian region: geodynamical constraints from observed rheological heterogeneities, Geophys. J. Int., 146, 760–780, https://doi.org/10.1046/j.1365-246X.2001.00492.x, 2001.

Ding G., Tian Q., Kong F., Xie X., Zhang L., and Wang L.: Segmentation of active fault, Seismological Press, Beijing, 1993.

490 Du F., Wen X., Feng J., Liang M., Long F., and Wu J.: Seismo-tectonics and seismic potential of the Liupanshan fault zone (LPSFZ), China, Chinese J. Geophys. Ch., 61, 545–559, https://doi.org/10.6038/cjg2018L018, 2018.

Du P.: Studying on the active characteristics and paleoearthquake of the eastern piedmont fault of Helan Mountain in the late Quaternary, M.S. thesis, China University of Geosciences (Beijing), Beijing, 2010.

Gan W., and Liu B.: Probability of large earthquake recurrence along the Jingtai-Tianzhu active fault, Seismology

495 And Geology, 24, 45–58, 2002.

Gao Z.: Late Quaternary activity characteristics and risk analysis of large earthquakes of the Zhuozishan West Piedmont Fault, M.S. thesis, Lanzhou Institute of Seismology, China Earthauake Administration, Lanzhou, 2020.

Guo P., Han Z., Gao F., Zhu C., and Gai H.: A new tectonic model for the 1927 M8.0 Gulang Earthquake on the NE Tibetan Plateau, Tectonics, 39, e2020TC006064, https://doi.org/10.1029/2020TC006064, 2020.

500 Guo P., Han Z., Mao Z., Xie Z., Dong S, Gao F. and Gai H.: Paleoearthquakes and rupture behavior of the Lenglongling Fault: implications for seismic hazards of the northeastern margin of the Tibetan Plateau, J. Geophys. Res. Sol. Ea., 124, 1520–1543, https://doi.org/10.1029/2018JB016586, 2019.

Hao M., Li Y., Wang Q., Zhuang W., and Qu W.: Present-day crustal deformation within the Western Qinling mountains and its kinematic implications, Surv. Geophys., 42, 1–19, https://doi.org/10.1007/s10712-020-09621-

505 5, 2021.

He J., Lu S., and Wang W.: Three-dimensional mechanical modeling of the GPS velocity field around the northeastern Tibetan plateau and surrounding regions, Tectonophysics, 584, 257–266, https://doi.org/10.1016/j.tecto.2012.03.025, 2013.

He W., Liu B., Yuan D., and Yang M.: Research on slip rates of the Lenglongling active fault zone, Northwestern

510 Seismological Journal, 22, 90–97, 2000.

He W., Yuan D., Ge W., and Luo H.: Determination of the slip rate of the Lenglongling fault in the middle and eastern segments of the Qilian mountain active fault zone, Earthquake, 30, 131–137, https://doi.org/ 10.3969/j.issn.1000-3274.2010.01.015, 2010.

He X., Wang D., and Wan F.: Discussion on the characteristics of the fracture zone of the Lanzhou M7.0 earthquake

515 in 1125 and the problems concerned, North China Earthquake Sciences, 15, 37–44, 1997.

Hergert T.: Numerical modelling of the absolute stress state in the Marmara Sea region - a contribution to seismic hazard assessment, PH.D thesis, Universität Karlsruhe, Karlsruhe, 2009.

Hergert T., and Heidbach O.: Slip-rate variability and distributed deformation in the Marmara Sea fault system, Nat. Geosci., 3, 132–135, https://doi.org/10.1038/ngeo739, 2010.

520 Hergert T., and Heidbach O.: Geomechanical model of the Marmara Sea region-II. 3-D contemporary background stress field, Geophys. J. Int., 185, 1090–1102, https://doi.org/10.1111/j.1365-246X.2011.04992.x, 2011.

Hergert T., Heidbach O., Bécel A., and Laigle M.: Geomechanical model of the Marmara Sea region-I. 3-D contemporary kinematics, Geophys. J. Int., 185, 1073–1089, https://doi.org/10.1111/j.1365-246X.2011.04991.x, 2011.

525   Hou K., Yuan D., and Li S.: Segmentation and deformation characteristics of Wuwei-Tianzhu-Zhuanglanghe fault zone, Crustal Deformation And Earthquake, 19, 55–63, 1999.

Hubert-Ferrari, A., King G., Manighetti I., Armijo R., Meyer B., and Tapponnier P.: Long-term elasticity in the continental lithosphere; modelling the Aden Ridge propagation and the Anatolian extrusion process, Geophys. J. Int., 153, 111–132, https://doi.org/10.1046/j.1365-246X.2003.01872.x, 2003.

530   Jamison D. B., and Cook N. G. W.: Note on measured values for the state of stress in the Earth's crust, J. Geophys. Res. Sol. Ea., 85, 1833–1838, https://doi.org/10.1029/JB085iB04p01833, 1980.

Jia W., Liu H., Liu Y., and Yuan D.: Preliminary study on activity of the Wudu-Kangxian fault zone, Northwestern Seismological Journal, 34, 142–149, 2012.

Laske G., Masters G., Ma Z., and Mike P.: Update on CRUST1.0 - A 1-degree Global Model of Earth's Crust,
535   Geophysical Research Abstracts, 15, Abstract EGU2013-2658, 2013.

Lasserre C., Morel P. H., Gaudemer Y., Tapponnier P., Ryerson F. J., King G. C. P., Métivier F., Kasser M., Kashgarian M., Liu B., Lu T., Yuan D.: Postglacial left slip rate and past occurrence of M≥8 earthquakes on the Western Haiyuan Fault, Gansu, China, J. Geophys. Res. Sol. Ea., 104, 17633–17651, https://doi.org/10.1029/1998JB900082, 1999.

540   Lease R. O., Burbank D. W., Zhang H., Liu J., and Yuan D.: Cenozoic shortening budget for the northeastern edge of the Tibetan Plateau: Is lower crustal flow necessary? , Tectonics, 31, TC3011, https://doi.org/10.1029/2011TC003066, 2012.

Lei J.: Research on activity of the West Helanshan fault, M.S. thesis, The Institute of Crustal Dynamics, China Eearthquake Administration, Beijing, 2015.

545   Lei Q., Chai C., Du P., Wang Y., and Meng G.: Activity characteristics of Luhuatai buried fault since late quaternary revealed by drilling, Seismology And Geology, 33, 602–614, https://doi.org/ 10.3969 /j.issn.0253-4967.2011.03.010, 2011.

Lei Q., Chai C., Meng G., Du P., Wang Y., Xie X., and Zhang X.: Composite drilling section exploration of Yinchuan buried fault, Seismology And Geology, 30, 250–263, 2008.

550   Lei Q., Chai C., Zheng W., Du P., Xie X., Wang Y., Cui J., Meng G.: Activity and slip rate of the northern section of Yellow River fault revealed by drilling, Seismology And Geology, 36, 464–477, https://doi.org/10.3969/j.issn.0253-4967.2014.02.015, 2014.

Lei Q.: The extension of the Arc Tectonic Belt in the Northeastern margin of the Tibet Plateau and the evolution of the Yinchuan Basin in the western margin of the North China, PH.D thesis, Institute of Geology, China Earthquake
555   Administration, Beijing, 2016.

Lei Q., Zhang P., Zheng W., Chai C., Wang W., Du P., and Yu J.: Dextral strike-slip of Sanguankou-Niushoushan fault zone and extension of arc tectonic belt in the northeastern margin of the Tibet Plateau, Sci. China Earth Sci., 59, 1025–1040, https://doi.org/10.1007/s11430-016-5272-1, 2016.

Liang M., Yuan D., Liu B., and Lei Z.: Seismic risk estimates for the Maxianshan north-margin fault, Northwestern
560   Seismology Journal, 30, 337–343, https://doi.org/10.3969/j.issn.1000-0844.2008.04.006, 2008.

Li C.: Quantitative studies on major active fault zones in Northeastern Qinghai-Tibet Plateau, PH.D. thesis, Institute of Geology, China Earthquake Administration, Beijing, 2005.

Li C.: The long-term faulting behavior of the eastern segment (Maqin-Maqu) of the east Kunlun fault since the late quaternary, PH.D. thesis, China Earthquake Administration, Beijing, 2009.

565   Li C., Zhang P., Yin J., and Min W.: Late Quaternary left-lateral slip rate of the Haiyuan fault, northeastern margin of the Tibetan Plateau, Tectonics, 28, TC5010, https://doi.org/10.1029/2008TC002302, 2009.

Li H., Xue L., Brodsky E. E., Mori J. J., Fulton P. M., Wang H., Kano Y., Yun K., Harris R. N., Gong Z., Li C., Si J., Sun Z., Pei J., Zheng Y., Xu Z.: Long-term temperature records following the Mw 7.9 Wenchuan (China) earthquake are consistent with low friction, Geology, 43, 163–166, https://doi.org/10.1130/G35515.1, 2015.

570   Li J., Cai Y., and Zhang J.: Geometric structure and slip gradient model of the Tazang fault in the east Kunlun fault zone, Earthquake, 39, 20–28, 2019.

Li L., Li X., Li M., Liang Z., Tian J., Zeng Z., Zeng X, Yan G., Lu M., Yang F., and Tan Z.: Spatial variability of modern tectonic stress fields in the north-eastern margin of Tibetan Plateau, Geol. J., 55, 7167–7192, https://doi.org/10.1002/gj.3818, 2020.

575   Li X., Pierce I. K. D., Bormann J. M., Hammond W. C., Zhang Z., Li C., Zheng W., and Zhang P.: Tectonic deformation of the Northeastern Tibetan Plateau and its surroundings revealed with GPS block modeling, J. Geophys. Res. Sol. Ea., 126, e2020JB020733, https://doi.org/10.1029/2020JB020733, 2021.

Li X., Hergert T., Henk A., and Zeng Z.: Contemporary kinematics in the eastern Tibetan Plateau: Insights from 3D geomechanical modeling, Tectonophysics, 819, 229109, https://doi.org/10.1016/j.tecto.2021.229109, 2021.

580   Li X., Hergert T., Henk A., and Zeng Z.: Contemporary background stress field in the eastern Tibetan Plateau: Insights from 3D geomechanical modeling, Tectonophysics, 822, 229177, https://doi.org/10.1016/j.tecto.2021.229177, 2022.

Li X., Li C., Pierce I. K. D., Zhang P., Zheng W., Dong J., Chen G., Ai M., Ren G., and Luo Q.: New slip rates for the Tianjingshan fault using optically stimulated luminescence, GPS, and paleoseismic data, NE Tibet, China. 585   Tectonophysics, 755, 64–74, https://doi.org/10.1016/j.tecto.2019.02.007, 2019.

Li X., Li C., Wesnousky S. G., Zhang P., Zheng W., Pierce I. K. D., and Wang X.: Paleoseismology and slip rate of the western Tianjingshan fault of NE Tibet, China, J. Asian Earth Sci., 146, 304–316, https://doi.org/10.1016/j.jseaes.2017.04.031, 2017.

Li X., Zhang P., Zheng W., Feng X., Li C., Pierce I. K. D., Xu H., Li X., Ai M., Chen G., Dong J., Liu J., and Ren G.: 590   Kinematics of late quaternary slip along the Qishan-Mazhao fault: implications for tectonic deformation on the southwestern Ordos, China, Tectonics, 37(9), 2983–3000, https://doi.org/10.1002/2018TC005043, 2018.

Li Y., Nocquet J. M., and Shan X.: Crustal deformation across the western Altyn Tagh fault (86° E) from GPS and InSAR, Geophys. J. Int., 228, 1361–1372, https://doi.org/10.1093/gji/ggab403, 2022.

Li Y., Nocquet J. M., Shan X., and Song X.: Geodetic observations of shallow creep on the Laohushan-Haiyuan Fault, 595   Northeastern Tibet, J. Geophys. Res. Sol. Ea., 126, https://doi.org/10.1029/2020JB021576, 2021.

Li Y., Ran R., Wang H., and Wu F.: Paleoseismic records of large earthquakes on the cross-basin fault in the salt lake pull-apart basin and cascade rupture events on the Haiyuan fault, Seismology And Geology, 38(4), 830–843, https://doi.org/10.3969/j.issn.0253-4967.2016.04.003, 2016.

Li Y., Shan X., Qu C., Zhang Y., Song X., Jiang Y., Zhang G., Nocquet J. M., Gong W., Gan W., and Wang C.: Elastic block and strain modeling of GPS data around the Haiyuan-Liupanshan fault, northeastern Tibetan Plateau, J. Asian Earth Sci., 150, 87–97, https://doi.org/10.1016/j.jseaes.2017.10.010, 2017.

Liu J., Ren Z., Zhang H., Li C., Zhang Z., Zheng W., Li X., and Liu C.: Late quaternary slip rate of the Laohushan fault within the Haiyuan fault zone and its tectonic implications, Chinese J. Geophys. Ch., 61, 1281–1297, https://doi.org/10.6038/cjg2018L0364, 2018.

Liu B., Feng S., Ji J., Wang S., Zhang J., Yuan H., and Yang G.: Lithospheric structure and faulting characteristics of the Helan Mountains and Yinchuan Basin: Results of deep seismic reflection profiling, Sci. China Earth Sci., 60, 589–601, https://doi.org/10.1007/s11430-016-5069-4, 2017.

Liu X., Yuan D., Shao Y., and Wu Z. Characteristics of late quaternary tectonic activity in the middle-eastern segment of the southern branch of Diebu-Bailongjiang fault, Gansu, Journal of Earth Sciences and Environment, 37, 111–119, https://doi.org/10.3969/j.issn.1672-6561.2015.06.010, 2015.

Liu-Zeng J., Shao Y., Klinger Y., Xie K., Yuan D., and Lei Z.: Variability in magnitude of paleoearthquakes revealed by trenching and historical records, along the Haiyuan Fault, China, J. Geophys. Res. Sol. Ea., 120, 8304–8333, https://doi.org/10.1002/2015JB012163, 2015.

Liu Z., Tian X., Gao R., Wang G., Wu Z., Zhou B., Tan P., Nie S., Yu G., Zhu G., and Xu X.: New images of the crustal structure beneath eastern Tibet fromahigh-density seismic array, Earth Planet Sc. Lett., 480, 33–41, https://doi.org/10.1016/j.epsl.2017.09.048, 2017.

Ma X., Yin G., Wei C., Qiang X., Ma Y., Liu C., Zhao Z., Gong L., Wang L., Ji H., Bai M., Mao J., and Li G.: High-resolution late Pliocene-quaternary magnetostratigraphy of the Yinchuan Basin, NE Tibetan Plateau, Quatern. Int., 607, 120–127, https://doi.org/10.1016/j.quaint.2021.09.009, 2021.

Matrau R., Klinger Y., Van der Woerd J., Liu-Zeng J., Li Z., Xu X., and Zheng R.: Late Pleistocene-Holocene Slip Rate Along the Hasi Shan Restraining Bend of the Haiyuan Fault: Implication for Faulting Dynamics of a Complex Fault System, Tectonics, 38, 4127–4154, https://doi.org/10.1029/2019TC005488, 2019.

Meade B. J., and Loveless J. P.: Block modeling with connected fault-network geometries and a linear elastic coupling estimator in spherical coordinates, B. Seismol. Soc. Am., 99, 3124–3139, https://doi.org/10.1785/0120090088, 2009.

Meng X., Shi L., Guo L., Tong T., and Zhang S. Multi-scale analyses of transverse structures based on gravity anomalies in the northeastern margin of the Tibetan Plateau, Chinese J. Geophys., https://doi.org/10.6038/j.issn.0001-5733.2012.12.006, 2012.

Min W., Jiao D., Chai C., Zhang P., and Mao F.: Characteristics of the active Luoshan Fault since Late Pleistocene, North Central China, Ann. Geophys., 46, 997–1013, https://doi.org/10.4401/ag-3442, 2003.

Ningxia Institute of Geolgocical Survey (NIGS): Regional geology of Ningxia Hui Autonomous Region, Geological Publishing House, Beijing, 2017.

Pang Y., Cheng H., Zhang H., and Shi Y.: Numerical analysis of the influence of lithospheric structure on surface vertical movements in Eastern Tibet, Chinese J. Geophys. Ch., 62, 1256–1267, https://doi.org/10.6038/cjg2019M0555, 2019a

Pang Y., Yang S., Li H., Cheng H., and Shi Y.: Numerical modeling of current crustal stress state in Haiyuan-Liupanshan fault system of NE Tibet, Acta Petrol. Sin., 35, 1848–1856, https://doi.org/10.18654/1000-0569/2019.06.13, 2019b.

Purcaru G., and Berckhemer H.: A magnitude scale for very large earthquakes, Tectonophysics, 49, 189–198, https://doi.org/10.1016/0040-1951(78)90177-4, 1978.

Rajabi M., Heidbach O., Tingay M., and Reiter K.: Prediction of the present-day stress field in the Australian continental crust using 3D geomechanical-numerical models, Aust. J. Earth Sci., 64, 435–454, https://doi.org/10.1080/08120099.2017.1294109, 2017.

Reiter K., and Heidbach O.: 3-D geomechanical–numerical model of the contemporary crustal stress state in the Alberta Basin (Canada), Solid Earth, 5, 1123–1149, https://doi.org/10.5194/se-5-1123-2014, 2014.

Ren J., Xu X., Yeats R. S., and Zhang S.: Millennial slip rates of the Tazang fault, the eastern termination of Kunlun fault: Implications for strain partitioning in eastern Tibet, Tectonophysics, 608, 1180–1200, https://doi.org/10.1016/j.tecto.2013.06.026, 2013.

Royden L. H., Burchfiel B. C., King R. W., Wang E., Chen Z., Shen F., and Liu Y.: Surface Deformation and Lower Crustal Flow in Eastern Tibet, Science, 276, 788–790, https://doi.org/10.1126/science.276.5313.788, 1997.

Shen Z., Sun J., Zhang P., Wan Y., Wang M., Bürgmann R., Zeng Y., Gan W., Liao H., and Wang Q.: Slip maxima at fault junctions and rupturing of barriers during the 2008 Wenchuan earthquake, Nat. Geosci., 2, 718–724, https://doi.org/10.1038/ngeo636, 2009.

Sheorey P. R.: A Theory for In Situ Stresses in Isotropic and Transversely Isotropic Rock, Int. J. Rock Mech. Min., 31, 23–34, 1994.

Shi Z., Li Y., Yuan D., Liu X., Ding X., and Geng S.: The recent active time of the south segment of the eastern Liupanshan piedmont fault: constraints from the characteristics of rhythmic deposits in the fault grooves, Acta Geoscientica Sinica, 35, 31–37, https://doi.org/10.3975/cagsb.2014.01.05, 2014.

Shi Z., Yuan D., Li T., Geng S., Lei Z., Liu X., He W., and Jin Q.: Textual research of A.D. 600 Qin-Long earthquake and discussion on its seismogenic structure, Science & Technology Review, 31, 48–52, https://doi.org/10.3981/j.issn.1000-7857.2013.12.008, 2013.

Song F., Yuan D., Chen G., Cheng J., Zhang L., He W., Ge W., Su H., and Lu B. Geometric structures and recent activity along the northwest segment of north marginal fault of Maxianshan mountains, Gansu province, Seismology And Geology, 28, 547–560, https://doi.org/10.3969/j.issn.0253-4967.2006.04.003, 2006.

Stromeyer, D., Heidbach, O., and Ziegler, M.: Tecplot 360 Add-on GeoStress v2.0. V. 2.0. GFZ Data Services, https://doi.org/10.5880/wsm.2020.001, 2020.

Sun Y., and Luo G.: Spatial-temporal migration of earthquakes in the northeastern Tibetan Plateau: insights from a finite element model, Chinese J. Geophys. Ch., 61, 2246–2264, https://doi.org/10.6038/cjg2018L0401, 2018.

Sun Y., Luo G., Yin L., and Shi Y.: Migration probability of big earthquakes and segmentation of slip rates on the fault system in northeastern Tibetan Plateau, Chinese J. Geophys. Ch., 62, 1663–1679, https://doi.org/10.6038/cjg2019M019, 2019.

Tapponnier P., Peltzer G., Le Dain A. Y., Armijo R., and Cobbold P.: Propagating extrusion tectonics in Asia: new insights from simple experiments with plasticine, Geology, 10, 611–616, https://doi.org/10.1130/0091-7613(1982)10<611:PETIAN>2.0.CO;2, 1982.

Tian J., Li M., Liang Z., Li L., Yan G., Lu M., and Tan Z.: Tectonic evolution of the Qingshuihe Basin since the Late Miocene: Relationship with north-eastward expansion of the Tibetan Plateau, Geol. J., 55, 7148-7166, https://doi.org/10.1002/gj.3650, 2020.

The Research Group on Active Fault Systems around the Ordos Massif (RGAFSAO).: Active fault system around Ordos Massif, Seismological Press, Beijing, 1988.

Wang C., Flesch L. M., Silver P. G., Chang L., and Chan W. W.: Evidence for mechanically coupled lithosphere in central Asia and resulting implications, Geology, 36, 363–366, https://doi.org/10.1130/G24450A.1, 2008.

Wang K.: On the strength of subduction megathrusts, Chinese J. Geophys., 64, 3452–3465, https://doi.org/10.6038/cjg2021P0515, 2021.

Wang M. and Shen Z. Present-Day Crustal Deformation of Continental China Derived From GPS and Its Tectonic Implications, J. Geophys. Res. Sol. Ea., 125, e2019JB018774, https://doi.org/10.1029/2019JB018774, 2020.

Wang S. Tectonic deformation in late Cenozoic of Liupanshan-Baoji fault zone in the NE margin of Tibet Plateau, PH.D thesis, Northwest University, Xi'an, 2018.

Wang S., Liu B., Tian X., Liu B., Song X., Deng X., Sun Y., Ma C., and Yang Y.: Crustal P-wave velocity structure in the northeastern margin of the Qinghai-Tibetan Plateau and insights into crustal deformation, Sci. China Earth Sci., 61, 1221–1237, https://doi.org/10.1007/s11430-017-9227-7, 2018.

Wang S., Shi Y., Feng X., and Tian Z.: Late Quaternary sinistral strike-slipping of the Liupanshan-Baoji fault zone: Implications for the growth of the northeastern Tibetan Plateau, Geomorphology, 380, 107628, https://doi.org/10.1016/j.geomorph.2021.107628, 2021.

Wang W., Qiao X., Yang S., and Wang D.: Present-day velocity field and block kinematics of Tibetan Plateau from GPS measurements, Geophys. J. Int., 208, 1088–1102, https://doi.org/10.1093/gji/ggw445, 2017.

Wang W., Zhang P., Kirby E., Wang L., Zhang G., Zheng D., and Chai C.: A revised chronology for Tertiary sedimentation in the Sikouzi basin: Implications for the tectonic evolution of the northeastern corner of the Tibetan Plateau, Tectonophysics, 505, 100–114, http://dx.doi.org/10.1016/j.tecto.2011.04.006, 2011.

Wang W., Zhang P., and Lei Q.: Deformational characteristics of the Niushoushan-Luoshan fault zone and its tectonic implications, Seismology and Geology, 35, 195–207, https://doi.org/10.3969/j.issn.0253-4967.2013.02.001, 2013.

Wang Y., and Liu B.: Analysis on seismic risk for faults in the mid-eastern Qilianshan area, Northwestern Seismological Journal, 23, 19–27, https://doi.org/10.3969/j.issn.1000-0844.2001.04.003, 2001.

Wu G., Tan H., Sun K., Wang J., Xi Y., and Shen C.: Characteristics and tectonic significance of gravity anomalies in the Helanshan-Yinchuan Graben and adjacent areas, Chinese J., Geophys., 63, 1002–1013, https://doi.org/10.6038/cjg2020N0233, 2020.

Xiao J., and He J.: 3D Finite-Element Modeling of Earthquake Interaction and Stress Accumulation on Main Active Faults around the Northeastern Tibetan Plateau Edge in the Past ~100 Years, B. Seismol. Soc. Am., 105, 2724-2735, https://doi.org/10.1785/0120140342, 2015.

Xu H., Wang H., and Cao J.: Slip rates of the major faults in the northeastern Tibetan Plateau and their geodynamic implications, Earthquake, 38, 13–23, 2018.

Xu X., Han Z., Yang X., Zhang S., Yu G., Zhou B., Li F., Ma B., Chen G., and Ran R. Seismotectonic Map in China and its Adjacent Regions, Seismological Press, Beijing, 2016.

Yang W., Zeng Z., Li D., Xing J., Wang J., and Luo W.: Three-level tectonic model for intraplate earthquakes, Earth Science Frontiers, 2009, 16, 206–217, 2009

Yang X. The study of the deformation characteristic of the Helanshan Tectonic Belts, PH.D thesis, Northwest University, Xi'an, 2018.

Ye Z., Gao R., Li Q., Zhang H., Shen X., Liu X., and Gong C.: Seismic evidence for the North China plate underthrusting beneath northeastern Tibet and its implications for plateau growth, Earth Planet. Sc. Lett., 426, 109–117, https://doi.org/10.1016/j.epsl.2015.06.024, 2015.

Ye Z., Li Q., Gao R., Zhang H., Shen X., Liu X., and Gong C.: Anisotropic regime across northeastern Tibet and its geodynamic implications, Tectonophysics, 671, 1–8, https://doi.org/10.1016/j.tecto.2016.01.011, 2016.

Yuan D., Liu B., Cai S., Liu X., and Wang Y.: Principal features of recent activity of the active northern marginal fault zone of Maxianshan mountains, Lanzhou, Gansu province, Seismology and Geology, 24, 315–323, https://doi.org/10.3969/j.issn.0253-4967.2002.03.003, 2002a.

Yuan D., Liu B., Zhang P., Liu X., Cai S., and Liu X.: The neotectonic deformation and earthquake activity in Zhuanglang river active fault zone of Lanzhou, Acta Seismologica Sinica, 24, 441–444, 2002b.

Yuan D., Liu X., Zheng W., Liu X., and Liu B.: Tectonic deformation feature and mechanism of the Maxianshan-Xinglongshan active fault system in the Lanzhou area, Earthquake Research In China, 19, 125–131, 2003.

Yuan D., Zhang P., Lei Z., Liu B., and Liu X.: A preliminary study on the new activity features of the Lajishan mountain fault zone in Qinghai province, Earthquake Research in China, 21, 93–102, 2005.

Yuan D., Lei Z., He W., Xiong Z., Ge W., Liu X., and Liu B.: Textual research of Wudu earthquake in 186 B.C. in Gansu Province, China and discussion on its causative structure, Acta Seismologica Sinica, 20, 696–707, 2007.

Zeng Z., Chen Z., Lu C., Yang Y., Chen K., Xiang S., Dai Q., Zhang J., Deng Y., Fu Y., Du Q., Liu L., and Yang W.: Earth system science research on earthquake mechanisms: Theory and validation of a new model, Earth Science Frontiers, 2021, 28, 263–282, https://doi.org/10.13745/j.esf.sf.2021.9.5, 2021.

Zhan Y., Zhao G., Wang J., Tang J., Chen X., Deng Q., Xuan F., and Zhao J.: Crustal electric structure of Haiyuan arcuate tectonic region in the northeastern margin of Qinghai-Xizang Plateau, China. Acta Seismologica Sinica, 27, 431–440, 2005.

Zhang P. Late quaternary tectonic deformation and earthquake hazard in continental China, Quaternary Sciences, 19, 404–413. https://doi.org/10.1088/0256-307X/15/11/025, 1999.

Zhang P., Deng Q., Zhang G., Ma J., Gan W., Min W., Mao F., and Wang Q.: Active tectonic blocks and strong earthquakes in the continent of China, Sci. China Ser. D, 46, 13–24, https://doi.org/10.1360/03dz0002, 2003.

Zhang P., Deng Q., Zhang Z., and Li H.: Active faults, earthquake hazards and associated geodynamic processes in continental China, Scientia Sinica Terrae, 43, 1607–1620, 2013.

Zhang P., Molnar P., Burchfiel B. C., Royden L., Wang Y., Deng Q., Song F., Zhang W., and Jiao D.: Bounds on the Holocene slip rate of the Haiyuan fault, North-Central China, Quaternary Res., 30, 151–164, https://doi.org/10.1016/0033-5894(88)90020-8, 1988.

Zhang P., Shen Z., Wang M., Gan W., Bürgmann R., Molnar P., Wang Q., Niu Z., Sun J., Wu J., Sun H., and You X.: Continuous deformation of the Tibetan Plateau from global positioning system data, Geology, 32, 809–812, https://doi.org/10.1130/G20554.1, 2004.

Zhang P., Zhang H., Zheng W., Zheng D., Wang W., and Zhang Z.: Cenozoic tectonic evolution of continental eastern Asia, Seismology And Geology, 36, 574–585, https://doi.org/10.3969 /j.issn.0253-4967.2014.03.003, 2014.

Zhang W., Jiao D., and Chai C.: The Tianjingshan active fault zone, Seismological Press, Beijing, 2015.

Zhang W., Jiao D., Zhang P. Molnar P., Burchfield, B. C., Deng Q., Wang Y., and Song F.: Displacement along the Haiyuan fault associated with the great 1920 Haiyuan, China, earthquake, B. Seismol. Soc. Am., 77, 117–131, 1987.

Zhang Z., McCaffrey R., and Zhang P.: Relative motion across the eastern Tibetan plateau: Contributions from faulting, internal strain and rotation rates, Tectonophysics, 584, 240–256, http://doi.org/10.1016/j.tecto.2012.08.006, 2013.

Zhao L., Zhan Y., Chen X., Yang H., and Jiang F.: Deep electrical structure of the central West Qinling orogenic belt and blocks on its either side, Chinese J. Geophys., 58, 2460–2472, https://doi.org/10.6038/cjg20150722, 2015.

Zheng W., Liu X., Yu J., Yuan D., Zhang P., Ge W., Pang J., and Liu B.: Geometry and late Pleistocene slip rates of the Liangdang-Jiangluo fault in the western Qinling mountains, NW China, Tectonophysics, 687, 1–13, https://doi.org/10.1016/j.tecto.2016.08.021, 2016a.

Zheng W., Yuan D., Zhang P., Yu J., Lei Q., Wang W., Zheng D., Zhang H., Li X., Li C., and Liu X.: Tectonic geometry and kinematic dissipation of the active faults in the northeastern Tibetan Plateau and their implications for understanding northeastward growth of the plateau, Quaternary Sciences, 36, 775–788, https://doi.org/10.11928/j.issn.1001-7410.2016.04.01, 2016b.

Zhou B., Peng J., and Zhang J.: Development and distribution patterns of active fault zones in Qinghai province, Journal of Engineering Geology, 17, 612–618, 2009.

Zhu A., Zhang D., and Jiang C.: Numerical simulation of the segmentation of the stress state of the Anninghe-Zemuhe-Xiaojiang faults, Sci. China Earth Sci., 59, 384–396, https://doi.org/10.1007/s11430-015-5157-8, 2016.

Zhu A., Zhang D., Zhu T., and Guo Y.: Influence of mantle convection to the crustal movement pattern in the northeastern margin of the Tibetan Plateau based on numerical simulation, Sci. China Earth Sci., 61, 1644–1658, https://doi.org/10.1007/s11430-017-9236-7, 2018.

Zhu S., and Zhang P.: A study on the dynamical mechanisms of the Wenchuan M_S8.0 earthquake, 2008, Chinese J. Geophys., 52, 418–427, 2009.